

# Simulating observations of dark matter dominated galaxies: towards the optimal halo profile

W. J. G. de Blok,<sup>1,2\*</sup> Albert Bosma<sup>3</sup> and Stacy McGaugh<sup>4</sup>

<sup>1</sup>*Australia Telescope National Facility, PO Box 76, Epping NSW 1710, Australia*

<sup>2</sup>*Department of Physics and Astronomy, Cardiff University, 5 The Parade, Cardiff CF24 3YB*

<sup>3</sup>*Observatoire de Marseille, 2 Place Le Verrier, 13248 Marseille Cedex 4, France*

<sup>4</sup>*Department of Astronomy, University of Maryland, College Park, MD 20742-2421, USA*

Accepted 2002 December 3. Received 2002 November 22; in original form 2002 July 29

## ABSTRACT

Low surface brightness galaxies are dominated by dark matter, and their rotation curves thus reflect their dark matter distribution. Recent high-resolution rotation curves suggest that their dark matter mass-density distributions are dominated by a constant-density core. This seems inconsistent with the predictions of cold dark matter (CDM) models which produce haloes with compact density cusps and steep mass-density profiles. However, the observationally determined mass profiles may be affected by non-circular motions, asymmetries and offsets between optical and dynamical centres, all of which tend to lower the observed slopes. Here we determine the impact of each of these effects on a variety of halo models, and we compare the results with observed mass-density profiles. Our simulations suggest that no single systematic effect can reconcile the data with the cuspy CDM haloes. The data are best described by a model with a soft core with an inner power-law mass-density slope  $\alpha = -0.2 \pm 0.2$ . However, no single universal halo profile provides a completely adequate description of the data.

**Key words:** galaxies: fundamental parameters – galaxies: kinematics and dynamics – dark matter.

## 1 INTRODUCTION

Low surface brightness (LSB) galaxies are dominated by dark matter. Their stellar populations are dynamically unimportant and the rotation curves are thus direct tracers of their dark matter distributions (de Blok & McGaugh 1997). This is important, as in brighter galaxies it is difficult to disentangle the dynamical contributions of the dark and visible matter, and unambiguously determine the distribution of the dark matter. LSB galaxies give us a unique opportunity to compare observations with cosmological dark matter simulations.

These numerical models, based on the cold dark matter (CDM) paradigm, make very specific predictions about the distribution of dark matter in galaxies (Dubinski & Carlberg 1991). In CDM haloes the mass-density distribution in the inner parts is characterized by a steep density ‘cusp’, usually described by a power law  $\rho(r) \sim r^\alpha$  with slopes varying from  $\alpha = -1$  (Navarro, Frenk & White 1996, 1997) to  $\alpha = -1.5$  (e.g. Moore et al. 1998, 1999; Bullock et al. 2001). This cusp manifests itself in a steeply rising rotation curve with a specific shape. Observations of dwarf and LSB galaxies (Moore 1994; McGaugh, Rubin & de Blok 2001; de Blok, McGaugh & Rubin 2001a; Blais-Ouellette, Amram & Carignan 2001; de Blok &

Bosma 2002; Marchesini et al. 2002) show that real rotation curves rise less steeply than predicted, and do not have the required CDM shape. Similar conclusions have been reached by Salucci (2001) and Salucci & Borriello (2001) for high surface brightness disc galaxies. At small radii, the empirically determined mass distribution can be well described by a central kpc-sized constant-density core (i.e.  $\alpha \sim 0$  in the inner parts) (de Blok et al. 2001b; de Blok & Bosma 2002, hereafter dBMBR and dBB02, respectively).

dBMBR and dBB02 base their conclusions on observations of rotation curves of over 60 LSB galaxies. They determine the mass-density profiles that give rise to the observed rotation curves and fit the inner parts with a single power law. The resulting distribution of inner mass-density slopes shows a strong peak at  $\alpha = -0.2 \pm 0.2$  (see figure 2 in dBMBR), but with a large spread, varying from steep and cuspy  $\alpha = -2$  profiles to flat and even moderately positive slopes. This was interpreted as a result of resolution effects; dBMBR find that the best resolved curves show the flattest profiles (see figure 3 in dBMBR and figure 14 in dBB02), contrary to what is expected for CDM. At lower resolutions, the CDM and the spherical pseudo-isothermal (ISO) models both predict the same slopes, leading to an ambiguity as to which model fits lower-resolution data best (van den Bosch & Swaters 2001).

However, resolution is not the only effect that can influence the measured slopes. Other effects, which dBMBR and dBB02 did not

\*E-mail: Erwin.deBlok@astro.cf.ac.uk

thoroughly investigate, include non-circular motions, offsets between dynamical and optical centres, lopsidedness, asymmetries, and slit-width. These effects all have the potential to decrease the measured inner mass-density slopes. It is thus important to investigate if the observed shallow slopes truly reflect the underlying mass distribution, or whether they are determined by systematic effects. For example, small offsets between the dynamical centre and the optical centre are sometimes observed in late-type barred galaxies (Pisano, Wilcots & Elmegreen 1998; de Vaucouleurs & Freeman 1972). If this were a systematic property of all LSB or dwarf galaxies then observations aligned on the optical centre would not necessarily probe the dynamical centre. Even if the galaxy in question had a steep CDM density cusp at the dynamical centre, the derived slope would be shallower, giving the impression of a core-dominated halo. Hence these systematic effects should be understood, in order to judge whether LSB galaxies have cuspy or core-dominated haloes. Furthermore, once the impact (if any) of these systematic effects is understood, we can hope to determine how much they contribute to the scatter in the observed slopes, and whether the range in observed slopes can be attributed to ‘cosmic scatter’ or whether a single halo profile for all galaxies suffices.

In this paper we investigate the importance of these systematic effects by deriving a large ensemble of rotation curves of both cuspy CDM and core-dominated (simulated) haloes, using observed curves as a constraint. We apply the relevant systematic effects to these simulated curves, and then determine the inner mass-density slopes. Our main conclusion is that none of the systematic effects investigated can convincingly wipe out the signature of a CDM halo. In other words, if LSB galaxies had CDM haloes, they would be unambiguously detectable, even in the presence of systematic effects. The most likely interpretation is that the observed core-dominated mass distribution reflects the true dark matter distribution in LSB galaxies.

The organization of this paper is as follows. In Section 2 we discuss some aspects of the observational comparison sample. In Section 3 we describe the simulations. Section 4 contains the results of simulations that include various systematic effects. In Section 5

we describe some tests performed with real data, while in Section 6 we attempt to use the simulations to improve on the halo model used. In Section 7 we present our conclusions.

## 2 DATA

The model rotation curves we derive will be compared with the results presented in dBMBR and dBBO2. The focus will be on the histograms of the inner slope  $\alpha$  (figure 2 of dBMBR) and the diagrams of inner slope  $\alpha$  versus resolution  $r_{\text{in}}$  of the rotation curve (figure 3 of dBMBR and figure 14 of dBBO2). These diagrams are based on power-law fits to the inner parts of the mass-density profiles derived from the  $\sim 60$  high-resolution rotation curves from McGaugh et al. (2001), de Blok et al. (2001a) and dBBO2. These rotation curves are measured from long-slit H $\alpha$  spectra, mostly sampling the kinematics in the inner parts, in many cases combined with lower-resolution H I rotation curves sampling the outer parts (de Blok, McGaugh & van der Hulst 1996).

### 2.1 Defining a restricted sample

These data span a large range in resolution, inclination, and general quality of the rotation curves. It is therefore worth asking whether the data themselves may in any way be biased by systematic effects. For example, if all the core-like profiles found turned out to have been derived from low-resolution, low-quality rotation curves, we would have valid reasons to question the usefulness of those data and the conclusions based on them.

McGaugh, Barker & de Blok (2003) present such an analysis where they analyse only those rotation curves that resemble Navarro–Frenk–White (NFW) CDM rotation curves best, and conclude that there is no systematic difference in the distributions of  $c$  for their restricted and total samples.

Here we make a similar comparison, but concentrate on the properties relevant for our comparison with simulations, namely distributions of  $c$  and the inner slope  $\alpha$ . Starting with the complete sample from dBMBR and dBBO2 (see Fig. 1), we apply the following cuts.

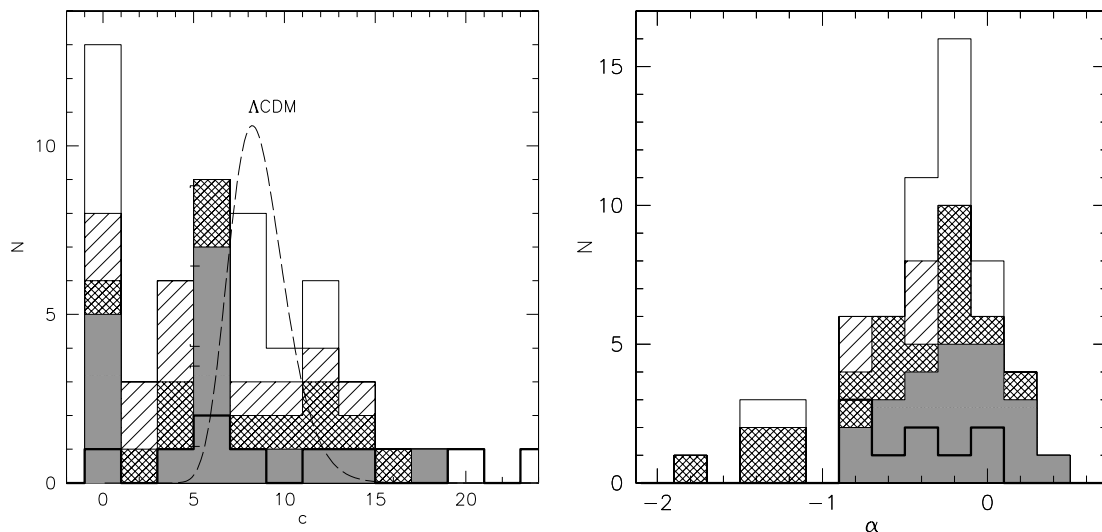


**Figure 1.** Distribution of the NFW concentration parameter  $c$  (left panel) and the inner mass-density slope  $\alpha$  (right panel) based on the data from dBMBR and dBBO2. The various superimposed histograms show the different stages of pruning: open histogram, full sample from dBBO2 and dBMBR; single-hatched histogram, galaxies with  $i < 30^\circ$  and  $> 85^\circ$  have been removed; double-hatched histogram, galaxies with low-quality rotation curves, asymmetries, etc., have been removed; grey-filled histogram, galaxies with less than two independent data points in the inner 1 kpc are removed. The thick-lined open histogram shows the restricted SMBB sample. The dashed curve in the left panel shows the expected distribution of  $c$  for a  $\Lambda$ CDM universe (e.g. McGaugh et al. 2003; Bullock et al. 2001).

**Table 1.** Restricted sample.

| Name           | Classification | Name      | Classification |
|----------------|----------------|-----------|----------------|
| F583-1         | U              | UGC 11648 | U              |
| F583-4         | U              | UGC 11748 | U              |
| ESO-LV 1200211 | U              | DDO 64    | U              |
| ESO-LV 2060140 | U              | DDO 185   | B              |
| ESO-LV 3020120 | B              | DDO 189   | U              |
| ESO-LV 4880490 | B              | NGC 1560  | U              |
| UGC 731        | B              | NGC 4395  | U              |
| UGC 3371       | U              | NGC 4455  | B              |
| UGC 4325       | U              | UGC 11583 | U              |
| UGC 11557      | D              |           |                |

‘B’ denotes barred; ‘U’ unbarred; ‘D’ dubious.

First, we remove all galaxies with inclinations  $i < 30^\circ$  and  $i > 85^\circ$ . This leaves 44 galaxies. The resulting distribution is insensitive to the choices for the upper and lower inclination limits. We have tried cuts with lower limits of  $25^\circ$  and  $40^\circ$ , and upper limits of  $75^\circ$  and  $80^\circ$ , and we find almost identical distributions. Secondly, we remove all galaxies with low-quality rotation curves, i.e. with a small number of independent data points, with large error bars, and large asymmetries. Galaxies where the minimum-disc assumption is clearly not valid were removed as well (e.g. UGC 6614). The resulting sample contains 39 galaxies. Finally, as the difference between cusp and core is most clearly visible in the innermost part of the galaxies, we demand that the inner part is resolved. We retain only those galaxies that have at least two independent data points in the inner 1 kpc. This leaves us with a final sample of 19 galaxies, listed in Table 1 and shown in Fig. 1.

A comparison of the different stages of pruning shows no systematic differences between the distributions of the initial full sample and the final restricted sample. If anything, the peak of the distribution of inner slopes  $\alpha$  has shifted towards a more positive value. The tail towards negative slopes has disappeared. The peak in the  $c$  distribution still occurs near  $c \sim 6$ , and the peak at  $c \sim 0$  is still present in the final sample.

## 2.2 Comparison with literature

Recently, Swaters et al. (2003, hereafter SMBB) have made a similar analysis of a sample of 15 dwarf and LSB galaxies. They reach the conclusion that the inner mass-density slopes in their sample cover the full range  $-1 \lesssim \alpha \lesssim 0$ , but claim that, although their data prefer a shallow  $\alpha \sim 0$  slope, they cannot rule out steep  $\alpha = -1$  slopes for their sample. The analysis presented in the previous section and in dBMBR suggests that a large fraction of the steep slopes found are actually due to insufficient resolution. It would thus be interesting to see if these effects are also present in the SMBB data. We subjected their data to the same quality criteria that we used for ours. In practice, this meant that five galaxies with less than two independent points in the inner kpc were rejected (F563-V2, F568-1, F568-3, F568-V1, F574-1), as well as one galaxy (U5721) where the minimum-disc assumption is invalid. A high-resolution optical velocity field of U5721 (Garrido et al. 2002) clearly shows the presence of a kinematical minor axis not perpendicular to the major axis. This is a classical indication of an oval distortion (Bosma 1978). For this galaxy, there are images in the *Hubble Space Telescope* (HST) archive that show the presence of a weak bar; see also dB02, their Section 9.2.2, noting that U5721 is also known as N3274.

We are thus left with nine well-resolved rotation curves. Our restricted sample has three galaxies in common with this restricted

SMBB sample. We find that for two of these galaxies the measured slopes are consistent at better than  $1\sigma$  (UGC 731 and UGC 4325). For one galaxy (UGC 11557) the slopes differ significantly – SMBB find  $\alpha = -0.84 \pm 0.27$ , while dBMBR find  $\alpha = -0.08 \pm 0.23$ . An inspection of the density profiles in figure 1 of dBMBR and figure 5 of SMBB shows that this difference in slope is entirely due to a different choice of break radius, where SMBB have chosen a larger radius than dBMBR, resulting in a much steeper slope. Choosing a smaller break radius will give a value entirely consistent with that in dBMBR. An inspection of the break radii of the eight other high-resolution SMBB profiles shows that UGC 11557 is the only case where we would claim that the choice in break radius is ambiguous. We have overplotted the distribution of slopes of the restricted SMBB sample in Fig. 1. The number of galaxies is small, so it is difficult to say anything about the intrinsic distribution of slopes, but it is clear that the SMBB sample is entirely consistent with our larger restricted sample (and even more so when the ambiguous slope for UGC 11577 is removed).

Contrary to the conclusions reached by SMBB we do not find that edge-on or barred galaxies skew the distribution of slopes. A comparison between our full and restricted samples shows that the inclusion or omission of edge-on galaxies does not shift the average value of the slope significantly from  $\alpha \sim -0.2$ . We also note that edge-on late-type galaxies are expected to be transparent (Bosma et al. 1992; Matthews & Wood 2001). Furthermore, the  $H\alpha$  spectra from which the rotation curves are derived do not show the broad velocity wings expected when projection effects play a large role.

Conclusions regarding the importance of bars are more ambiguous as these depend on what we define as a bar. Certainly none of the galaxies investigated here contains the dominant straight bars found in earlier-type galaxies. Here we are mostly dealing with Magellanic-type oval components, and it is obviously a matter of judgement to decide whether we deal with an intrinsically oval component, or a projected more circular one.

SMBB list which of the galaxies in their sample they consider barred. In order to make a consistent barred/non-barred division of the galaxies in our restricted sample, we use their results to gauge and calibrate our classification. That any such classification remains uncertain is illustrated by the fact that none of the galaxies in the SMBB sample is classified in the NASA/IPAC Extragalactic Database (NED) as unambiguously barred (Hubble type SB), *except* UGC 2259 [Hubble type SB(s)dm]. SMBB classify this galaxy as *unbarred*, even though the bar with perpendicular spiral arms is easily visible on the Digital Sky Survey image. The inner mass-density slope found for this galaxy is steep at  $\alpha = -0.86 \pm 0.18$ . As bars are disc dynamical features (e.g. Athanassoula 2002), they imply a significant disc mass. Such heavy discs more than compensate for any underestimate of the slope which might be caused by the non-circular motions they induce. The minimum-disc assumption fails, and with it the steep halo slopes inferred in this extreme limit.

Despite this UGC 2259 discrepancy, we have used the SMBB results to gauge which of the galaxies in our restricted sample should be classified as barred. We list our classification in Table 1; we find 13 non-barred galaxies, five barred galaxies and one ambiguous case.

The galaxies in our restricted sample have been selected not to suffer from inclination effects or projection effects. The majority of them are unbarred, and it is not obvious at all that the presence of a bar influences any of the results. This comparison of restricted samples shows that once a proper pruning is made to only include minimum-disc, well-resolved galaxies, most of the differences are merely a matter of semantics. The observed *shallow* inner

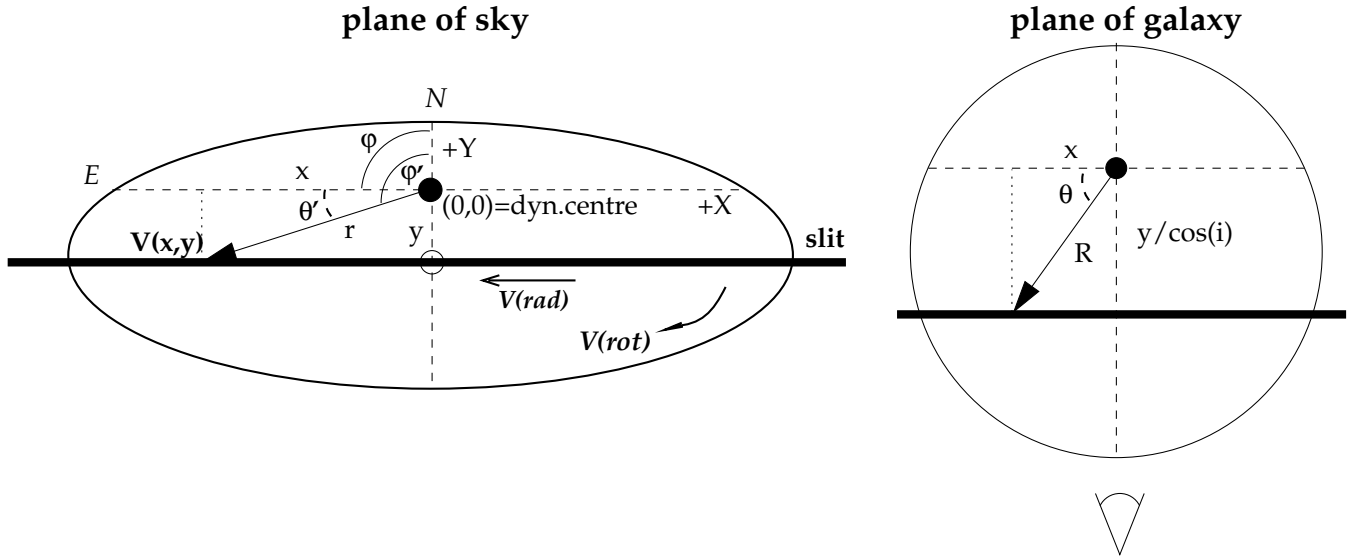


**Figure 2.** Schematic diagram of the geometry of an inclined rotating disc projected on the sky. All angles and distances are measured in the plane of the sky, except  $R$  and  $\theta$  which are measured in the plane of the galaxy. See text for more details.

mass-density slopes of LSB and dwarf galaxies do therefore reflect the intrinsic properties of their potentials.

### 3 MODELS

#### 3.1 Model rotation curves

In order to model the various effects that can affect rotation curves we use the full expression for the observed line-of-sight velocity at any position in a galaxy velocity field. This is given by (see Fig. 2):

$$V(x, y) = V_0 + V_C(R) \sin i \cos \theta + V_{\text{exp}}(R) \sin i \sin \theta. \quad (1)$$

Here  $V(x, y)$  is the observed velocity at position  $(x, y)$ , where we define the dynamical centre of the galaxy to be at  $(0, 0)$ ;  $V_0$  is the systemic velocity, which is not relevant in this analysis and which will be ignored;  $V_C(R)$  is the actual rotation curve velocity at radius  $R$ , where  $R$  is measured in the plane of the galaxy; and  $V_{\text{exp}}(R)$  is an expansion velocity describing non-circular motions (which can be used to describe, for example, streaming motions). Position  $(x, y)$  is measured in the plane of the sky. We additionally define the radius  $r$  as the projection of  $R$  on the plane of the sky. As usual,  $i$  is the inclination. Following Begeman (1987), we define a coordinate system with the  $+X$  direction towards decreasing right ascension, the  $+Y$  direction towards the north, and the dynamical centre as origin. Position angles in the plane of the sky are measured from  $N$  towards  $E$ . The major axis of the galaxy has sky position angle (PA)  $\phi$ . Position  $(x, y)$  then has PA  $\theta$  with respect to the major axis as measured in the plane of the galaxy given by:

$$\begin{aligned} \cos \theta &= \frac{-x \sin \phi + y \cos \phi}{R} \\ \sin \theta &= \frac{-x \cos \phi - y \sin \phi}{R \cos i}. \end{aligned} \quad (2)$$

We now introduce the angle  $\phi'$ , which is the sky PA of position  $(x, y)$ . We can express  $x$  and  $y$  as

$$\begin{aligned} x &= -r \cos \left( \frac{\pi}{2} - \phi' \right) = -r \sin \phi' \\ y &= r \sin \left( \frac{\pi}{2} - \phi' \right) = r \cos \phi'. \end{aligned} \quad (3)$$

Combining this with equation (2) gives

$$\cos \theta = \frac{r}{R} (\sin \phi' \sin \phi + \cos \phi' \cos \phi)$$

$$\sin \theta = \frac{r}{R \cos i} (\sin \phi' \cos \phi - \cos \phi' \sin \phi). \quad (4)$$

Without loss of generalization, we can make the simplifying assumption that the major axis coincides with the  $X$ -axis, so that  $\phi = \pi/2$ , as sketched in Fig. 2. Equation (4) then reduces to  $\cos \theta = (r/R) \sin \phi'$  and  $\sin \theta = -[r/(R \cos i)] \sin \phi'$ .

We are now in a position to derive the line-of-sight velocity at any position  $(x, y)$ , given any rotation curve  $V_C$  and non-circular motion component  $V_{\text{exp}}$ . For example, Fig. 2 shows a slit positioned parallel to the major axis, but offset by an amount  $y$ . Assuming that  $V_{\text{exp}} = 0$  everywhere, the observed line-of-sight velocities along the slit are derived by varying  $x$  at a constant  $y$ , for a given input  $V_C(R)$  and known  $i$ . The radii  $R = \sqrt{x^2 + (y/\cos i)^2}$  and  $r = \sqrt{x^2 + y^2}$  can be calculated, as can the PA  $\phi' = \arctan(y/x)$ , so that  $\theta$  can be derived. This then trivially gives the line-of-sight velocities. One last step we need to take, in order to ‘simulate’ our ignorance regarding the systematic effects in this particular example, is to associate the positions along the slit  $x$  (rather than the radii  $r$ ) with the derived line-of-sight velocities, because, as with real data, these curves will be analysed under the assumption that no systematic effects are present. Other situations, including non-circular motions, can be modelled in a similar way, as shown below.

#### 3.2 Halo models

For  $V_C(R)$  we will initially investigate two halo models, apply identical systematic effects to both, and determine the resulting rotation curves and mass-density profiles. The first model is the so-called NFW halo, favoured by the CDM simulations, but seemingly not by the observations. The other model is the pseudo-isothermal halo, preferred by observations, but without any basis in cosmology. The properties of these models are summarized below.

##### 3.2.1 NFW haloes

Navarro et al. (1996, 1997) have investigated in detail the internal structure of dark matter haloes formed in a CDM universe. They

found that the haloes modelled in their  $N$ -body simulations could be well described by

$$\rho(R) = \frac{\rho_i}{(R/R_s)(1 + R/R_s)^2} \quad (5)$$

where  $R_s$  is the characteristic radius of the halo and  $\rho_i$  is related to the density of the universe at the time of collapse. The density and radius are strongly correlated with the mass of the halo. At small radii the density diverges as  $r^{-1}$ . This mass distribution gives rise to a halo rotation curve

$$V_C(R) = V_{200} \left\{ \frac{\ln(1 + cx) - cx/(1 + cx)}{x[\ln(1 + c) - c/(1 + c)]} \right\}^{1/2}, \quad (6)$$

where  $x = R/R_{200}$ . The radius  $R_{200}$  is the radius where the density contrast exceeds 200, roughly the virial radius (Navarro et al. 1996). The characteristic velocity  $V_{200}$  of the halo is defined in the same way as  $R_{200}$ . The curve is characterized by two parameters: a concentration  $c$  and a velocity  $V_{200}$ . These are not independent, but are related through the assumed cosmology. For a standard  $\Lambda$ CDM this relation can be well described as

$$\log c = 1.191 - 0.064 \log V_{200} - 0.032 \log^2 V_{200} \quad (7)$$

(cf. Navarro et al. 1997). This relationship has an associated scatter, but estimates in the literature differ. Here we adopt a conservative logarithmic scatter of  $\sigma(\log c) = 0.18$  (Bullock et al. 2001). Note that, in a more recent paper, Wechsler et al. (2002) advocate a scatter of  $\sigma(\log c) = 0.14$ . As the precise value of the scatter is not critical for our results, we use the larger value in order to give the maximum amount of leeway to the CDM models. See de Blok et al. (2001a) for more details.

Recent  $N$ -body simulations have found even steeper inner mass-density slopes of  $\alpha = -1.5$  (Moore et al. 1998). We do not consider these steeper slopes here; the NFW model can be regarded as a limiting case. If the data do not admit  $\alpha = -1$  slopes, they certainly will not allow  $\alpha = -1.5$  values.

In Fig. 3 we show the inner part of the velocity field of a massless disc in a NFW halo with  $c = 8.6$  (i.e. approximately the typical value predicted by  $\Lambda$ CDM, see McGaugh et al. 2003) and  $V_{200} = 100 \text{ km s}^{-1}$ . The iso-velocity contours show a characteristic ‘pinch’ in the very inner parts, which is a signature of the NFW profile.

### 3.2.2 ISO haloes

The spherical ISO halo differs from the NFW halo in that it has a central region with a constant density. Its density profile is

$$\rho(R) = \frac{\rho_0}{1 + (R/R_C)^2}, \quad (8)$$

where  $\rho_0$  is the central density of the halo, and  $R_C$  is the core radius of the halo. The corresponding rotation curve is given by

$$V_C(R) = \sqrt{4\pi G \rho_0 R_C^2 [1 - (R_C/R) \arctan(R/R_C)]}. \quad (9)$$

The ISO halo is characterized by any two out of three parameters: an asymptotic velocity  $V_\infty$ , a core radius  $R_C$  and a central density  $\rho_0$ . These parameters are related through

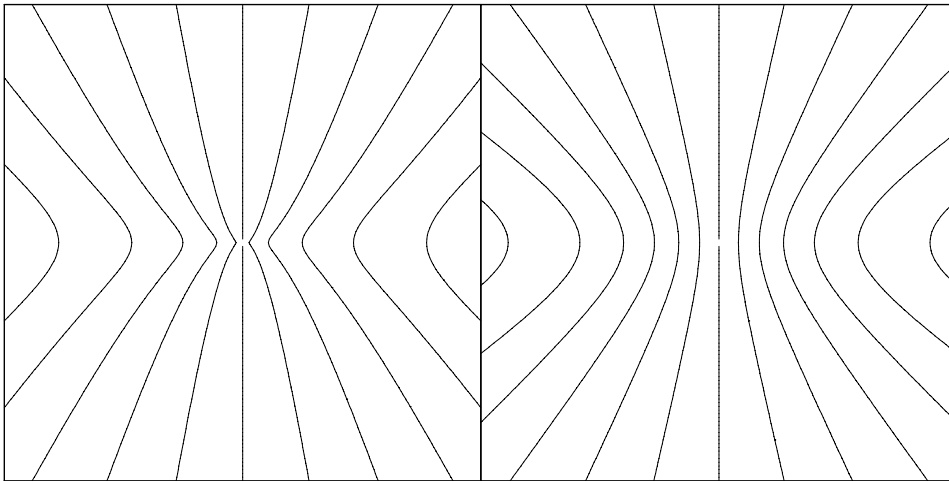
$$V_\infty = \sqrt{4\pi G \rho_0 R_C^2}. \quad (10)$$

Fig. 3 shows the inner part of a velocity field of a massless disc embedded in an ISO halo with  $V_\infty = 100 \text{ km s}^{-1}$  and  $R_C = 1 \text{ kpc}$ . The iso-velocity contours are much rounder, and do not show the ‘pinch’ of the NFW velocity field.

### 3.3 Simulations

In order to be able to directly compare the simulations with the data it is important that the simulated haloes are ‘realistic’, in the sense that the range of halo parameters for the NFW model needs to be similar to that found in the simulations (which are constructed to resemble the real Universe), whereas the ISO halo parameters need to resemble those determined from observations. We therefore use the following boundary conditions in the models.

(i) Halo parameters. For the NFW haloes we take a random value for  $V_{200}$  between between 20 and  $490 \text{ km s}^{-1}$ , and we compute the corresponding  $c$ -value using equation (7), modified by a random scatter as described above. To simulate ISO haloes we choose a random value for  $V_\infty$  between 30 and  $300 \text{ km s}^{-1}$ , roughly corresponding to the observed range in galaxy maximum rotation velocities. For  $\rho_0$  we choose a random value from the uniform range  $\log(\rho_0/[M_\odot \text{ pc}^{-3}]) = -1.7 \pm 0.4$  (Firmani et al. 2000). The core radius  $R_C$  is then determined using equation (10).



**Figure 3.** Velocity fields of the inner parts of massless discs embedded in a NFW halo (left panel) and an ISO halo (right panel). The velocity field is seen under an inclination angle of  $60^\circ$ , and a PA of  $90^\circ$ . The boxes measure  $5 \times 5 \text{ kpc}^2$ . The vertical minor-axis contour is  $0 \text{ km s}^{-1}$ , increasing in steps of  $10 \text{ km s}^{-1}$  outwards. The NFW halo parameters are  $c = 8.6$  and  $V_{200} = 100 \text{ km s}^{-1}$ , the ISO parameters are  $R_C = 1 \text{ kpc}$  and  $V_\infty = 100 \text{ km s}^{-1}$ .

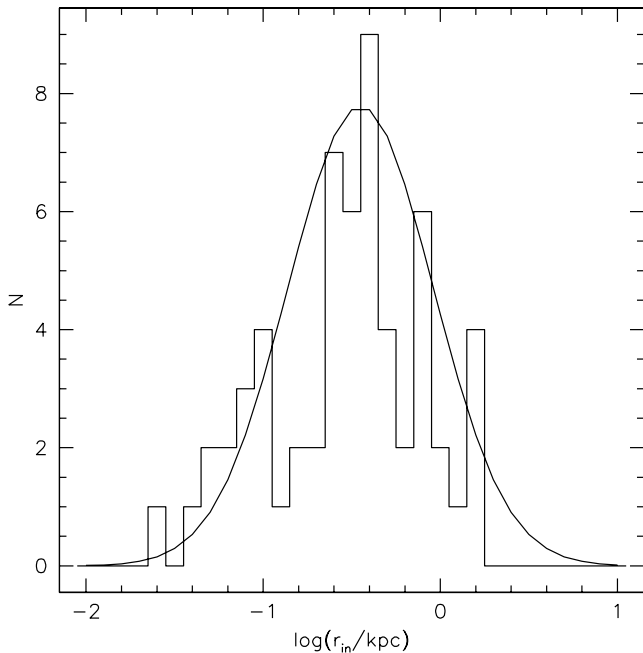


**Figure 4.** Distribution of the resolutions  $\log r_{\text{in}}$  of the rotation curves in presented in dBMBR and dB02. We overplot a Gaussian with average  $\mu(\log r_{\text{in}}) = -0.45$  and  $\sigma(\log r_{\text{in}}) = 0.41$  which was used as a probability distribution for the simulations.

(ii) Inclination. A random axial ratio is chosen in the range from 0.17 to 0.76, corresponding to inclinations between  $40^\circ$  and  $80^\circ$ . The inclination has no direct effect on the slopes, but serves as a scale factor in the error bars determined below, and hence the uncertainty in the slopes.

(iii) Physical resolution. For each simulated galaxy, the resolution in kpc at which it will be ‘observed’ is determined as follows. Fig. 4 shows the logarithmic distribution of observed resolutions (radii  $r_{\text{in}}$  of the innermost points of the rotation curves) from dBMBR and dB02. This distribution is well approximated by a Gaussian with an average  $\mu(\log r_{\text{in}}) = -0.45$  and a dispersion  $\sigma(\log r_{\text{in}}) = 0.41$ . The  $2\sigma$  spread in resolution thus varies from 0.05 to 2.3 kpc, reflecting both the spread in distance as well as the mix of optical and H I curves used. Although the precise parameters of this distribution are not critical, choosing a resolution distribution that is approximately equal to the empirical one means we can make a direct comparison between the simulations and observations.

(iv) Error bars. To simulate the uncertainties in the data, we de-correct the rotation curve for inclination and add error bars. Fig. 5 shows the distribution of the observational uncertainties in the dB02 data, not corrected for inclination. The best-fitting Gaussian has an average  $\mu(\log \Delta V) = 0.629$  and a dispersion  $\sigma(\log \Delta V) = 0.437$ . As in dB02 and de Blok et al. (2001a) we impose a minimum error of  $4 \text{ km s}^{-1}$  on the data. We draw error bars from this distribution and assign them to the data points in the simulated rotation curve. The curve is then corrected back for inclination, thus enlarging the error bars and uncertainty accordingly. As the intensity of the  $H\alpha$  line is generally inversely correlated with the magnitude of the error bar, this procedure assumes a random distribution of  $H\alpha$  intensities. This is likely to be simplistic, but any improvement involves assuming a specific  $H\alpha$  intensity distribution, meaning the models would lose some of their generality.

(v) Slit width. Equation (1) gives the line-of-sight velocities along an infinitely thin slit. In reality, the observations have used

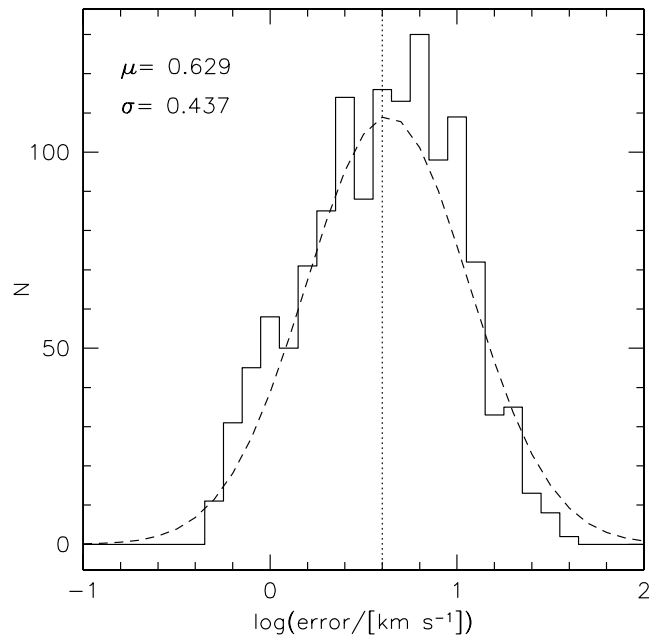


**Figure 5.** Distribution of the error bars in the unsmoothed rotation curves presented in dB02. We overplot a best-fitting Gaussian with  $\mu = 0.629$  and  $\sigma = 0.437$ . This was used as the probability distribution for assigning errors. The vertical line indicates the value of  $4 \text{ km s}^{-1}$ . Errors smaller than  $4 \text{ km s}^{-1}$  were set to be  $4 \text{ km s}^{-1}$ , in a similar way as the data.

a finite slit with a width of  $\sim 1$  arcsec. We therefore integrate equation (1) over a width of 1 arcsec and determine the average value of  $V(x, y)$  at each position along the thick slit.

(vi) Mass-density profiles. The mass-density profiles are determined exactly as described in dBMBR, with one difference. dBMBR choose a ‘break radius’ to determine the inner slope. Here we determine the slope by performing a weighted fit to the innermost three points. The uncertainty in the slope is determined in the same manner as in dBMBR. We have tested fitting to the innermost two, four or five points but this did not change any of the conclusions appreciably. We assume a spherical halo and minimum disc, i.e. the dynamical significance of the stellar disc is assumed to be negligible and the stellar mass-to-light is set to zero. For LSB galaxies minimum disc is in general a good assumption (e.g. de Blok & McGaugh 1997). It is difficult to estimate what effect the stellar disc has on the halo, but most likely the halo becomes more concentrated under the influence of the disc. In the absence of applicable models we will not explicitly simulate this, except to note that because of the dynamical insignificance of the disc the effect is likely to be small. The minimum-disc assumption also gives a hard upper limit on the value of the slope, as taking into account any contribution by the stars to the mass-density slope reduces the implied dark matter slope, independent of whether any contraction has taken place or not.

(vii) Small-scale deviations. The model rotation curves can by necessity be nothing more than pale imitations of those of real galaxies. One of the features of real rotation curves are the ‘bumps and wiggles’, caused by, among others, streaming motions along spiral arms, random motions of H II regions, and gas motions due to the effects of star formation. The magnitude and importance of these effects are of course different for different galaxies. They do undoubtedly play a role in the observed LSB galaxies rotation curves, but without modelling individual galaxies in detail it is

impossible to determine and apply these effects to the models in an unbiased and general manner. We return to this matter in Section 4.2. It should be noted though that the many ways in which rotation curves can be derived are all designed to remove the effects of these small-scale deviations. For example, the tilted ring procedure averages velocities over rings at a certain radius, whereas long-slit rotation curves use the independent information from radii at the approaching and receding sides of the galaxy to derive the underlying global rotation velocities. Our omission of these deviations means that the uncertainties we derive in our simulations will be smaller than found in the data, but this is a small price to pay for not having to introduce ill-constrained random motions that may bear no resemblance with reality. A specific example is discussed in Section 4.2.

## 4 RESULTS

### 4.1 Comparison with models

For each set of input parameters described below we compute 600 rotation curves per halo model. This is significantly more than the 61 observational data points available, but avoids small number statistics affecting the simulated histogram. To compare the data and the simulations we scale the maximum of the data histogram to that of the simulation histogram. To indicate the uncertainties in the data histogram we overplot an error bar on each observed histogram bin which reflects the uncertainty due to counting statistics in the observational sample (these error bars are also scaled); see Fig. 6 for examples. In the diagram of inner slope  $\alpha$  versus resolution

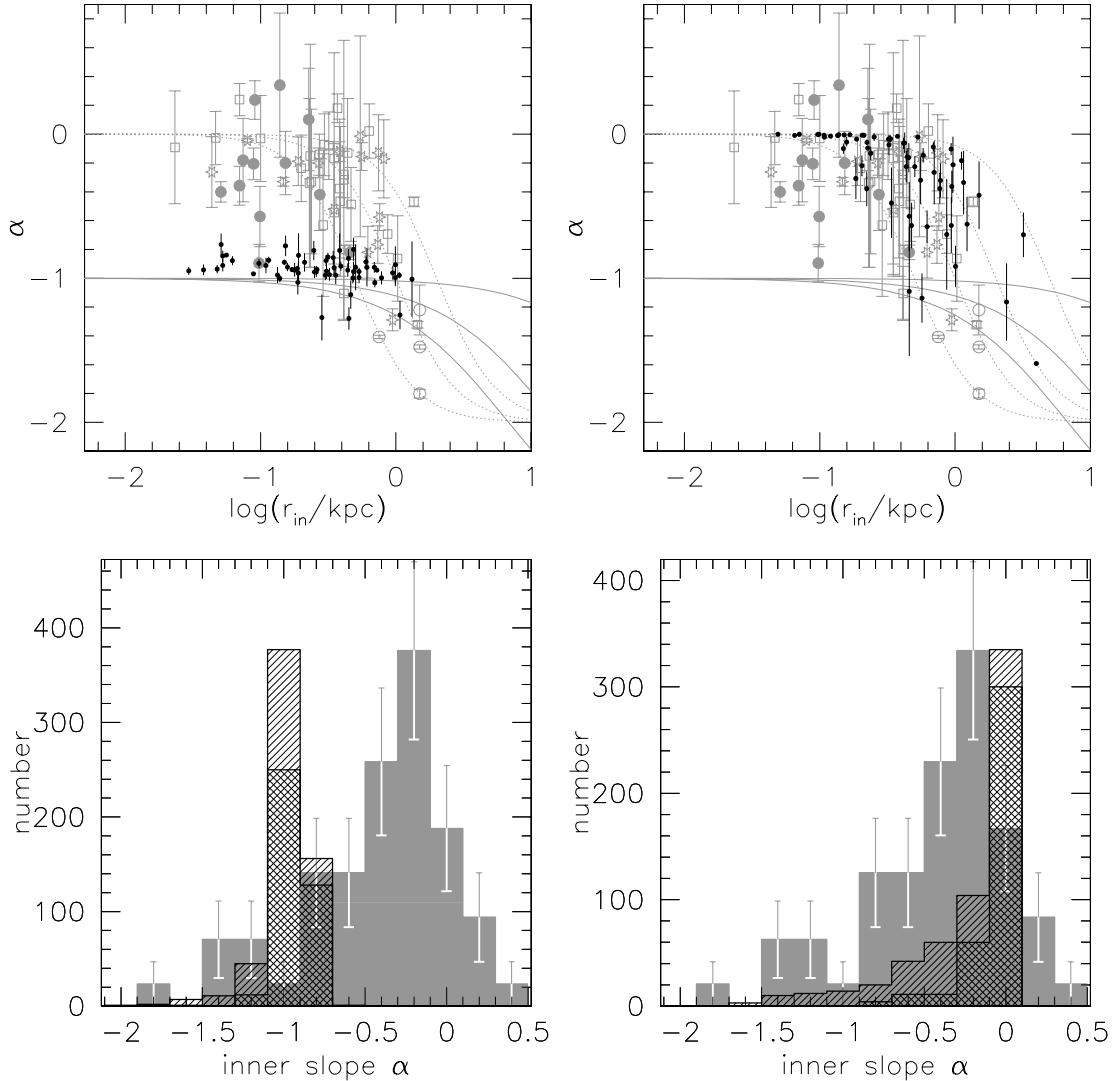


**Figure 6.** Comparison of the simulated NFW (left) and ISO (right) haloes. The top panels compare the simulated  $r_{\text{in}}-\alpha$  data points (black) with the observed distribution from dBMBR and dBBO2 (grey data points). No systematic effects are assumed. The grey dotted lines converging on  $\alpha = 0$  represent the theoretical variations in slope for ISO haloes with  $R_C = 0.5, 1$  and  $2$  kpc. The lines converging on  $\alpha = -1$  show the variation in slope for  $c/V_{200} = 9.8/50, 8.6/100$  and  $6.1/500$  (the slope only depends on the ratio  $c/V_{200}$ ). The bottom panels show the histograms of  $\alpha$  values for the two models. The double-hatched histogram indicates well-resolved galaxies with  $r_{\text{in}} \leq 0.5$  kpc.

$r_{\text{in}}$  we show observational data points in the background, with the simulation results overlotted. To avoid cluttering the plot we do not always show all 600 galaxies, but select 61 galaxies (i.e. equal to the number of observed data points) at random; see Fig. 6 for examples.

In order to isolate the investigated systematic effects from resolution effects, we distinguish in the histograms between well-resolved galaxies (two or more independent points per kpc; cross-hatched histogram) and less well-resolved galaxies (less than two independent points per kpc; single-hatched histograms). The cross-hatched histograms can be directly compared with the well-resolved sample in Fig. 1.

#### 4.2 The null case

We first investigate the case of observations without any systematic effects. That is, we determine the major-axis curves defined by equation (1) and the ISO and NFW halo models, and follow the procedure described in Section 3.3. We assume that there are no non-circular motions and no mismatches of any kind. The results are shown in Fig. 6. As expected, the derived slopes are close to the theoretical values. The NFW model shows a pronounced peak at  $\alpha = -1$ . The finite width of the slit hardly affects the measured slopes. Similar conclusions apply to the ISO model. The high-resolution ISO models show a clear  $\alpha = 0$  slope, while the least-resolved models show steeper slopes, comparable to those found in the NFW model at similar resolutions.

The histograms show only partial agreement with the data. The peak occurs at the wrong value for the NFW model, and the histogram has the wrong shape. For the ISO model, the peak occurs at roughly the correct value, but the shape of the histogram differs significantly from the data. Clearly some sort of effect, whether cosmic or systematic, is needed to make the simulations more consistent with the data. It is clear though that this effect needs to be more pronounced for NFW than for ISO.

##### 4.2.1 Small-scale deviations

The simulated error bars in Fig. 6 are smaller than those of the data. As discussed in item (vii) in Section 3.3, this is most likely due to the fact that we do not simulate small-scale features in the rotation curves. However, this does not affect the conclusions we can draw from the simulations. After all, when averaged over  $\sim 60$  rotation curves, we can regard the ‘bumps and wiggles’ as essentially random; they introduce scatter but are expected to average out and will not affect the shape in a systematic way. Another reason not to include the small-scale deviations is that every galaxy is unique and has features in the rotation curve that depend on the positions of the H II regions, spiral arms, star formation, etc. Given the low star-formation rates, the small number of H II regions and the lack of pronounced spiral arms, it is unclear how important any of these effects are in LSB galaxies compared to ‘normal’ galaxies. It is therefore difficult to derive a universally applicable description short of modelling each galaxy individually, which is clearly not feasible.

We illustrate the fact that small-scale deviations most likely do not affect the conclusions, but merely introduce more scatter, by investigating a naive (and probably too simplistic) description for the deviations which we then apply to the simulations presented above. Fig. 7 shows a histogram of the deviations of the raw observed rotation curves with respect to the smooth rotation curves as

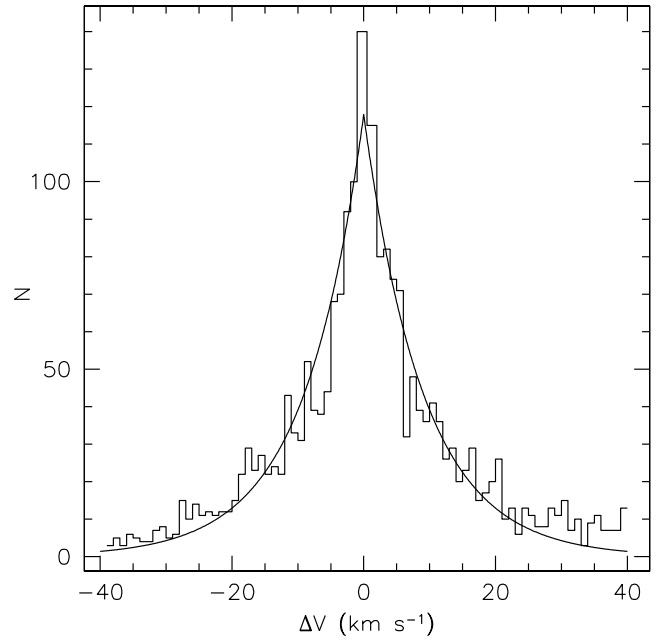


**Figure 7.** Histogram of the deviations of the raw data points from the underlying smooth rotation curves presented in de Blok et al. (2001a). The distribution is symmetrical, and can be well described by a function of the form  $N = 117.9 e^{-|\Delta V|/9.06}$ , as shown by the superimposed curve.

presented in figure 7 of dBB02 and figure 1 of de Blok et al. (2001a). The deviation histogram is well described by a function of the form  $\exp -|\Delta V|$ . If the deviations in the rotation curves were radially uncorrelated, we could add deviations derived from this distribution to our model curves, use this modified model curve to determine the underlying smooth rotation curve and subsequently measure the mass profile.

However, in real galaxies the small-scale deviations are correlated; if, for example, streaming motions along a (resolved) spiral arm cause a data point to lie above the average curve, then the data point next to it is more likely to lie above it as well. Furthermore, the deviations are defined with respect to the underlying curve, in that the latter is derived by minimizing the former. Ideally, we would have to introduce an extra step in the simulations to adjust the model rotation curves to the effect of the deviations. On the other hand, as we would afterwards be fitting to the underlying curve as defined by a minimization of deviations, and *not* to the raw deviations, their impact on the results would have to be significantly less than suggested by Fig. 7. It is thus not clear whether taking small-scale deviations into account would have a significant effect.

As a crude attempt to show these effects, to the two simulations described above we have applied small-scale deviations drawn from the distribution shown in Fig. 7. In order to introduce a degree of correlation between the deviations, we boxcar-smooth over four data points. With real data the next step would have been to fit an underlying smooth curve by minimizing the residuals, followed by the derivation of the mass profile from the smooth curve. To determine the mass profiles we thus prefer not to use the raw data, because the mass profile derivation uses the gradient of the rotation curve. Instead we introduce some binning and smoothing to determine the underlying gradient. In practice, we thus have to soften the impact of the derived (unbinned) deviations on the simulated curves. Here we (arbitrarily) divide them by a factor of 4 before

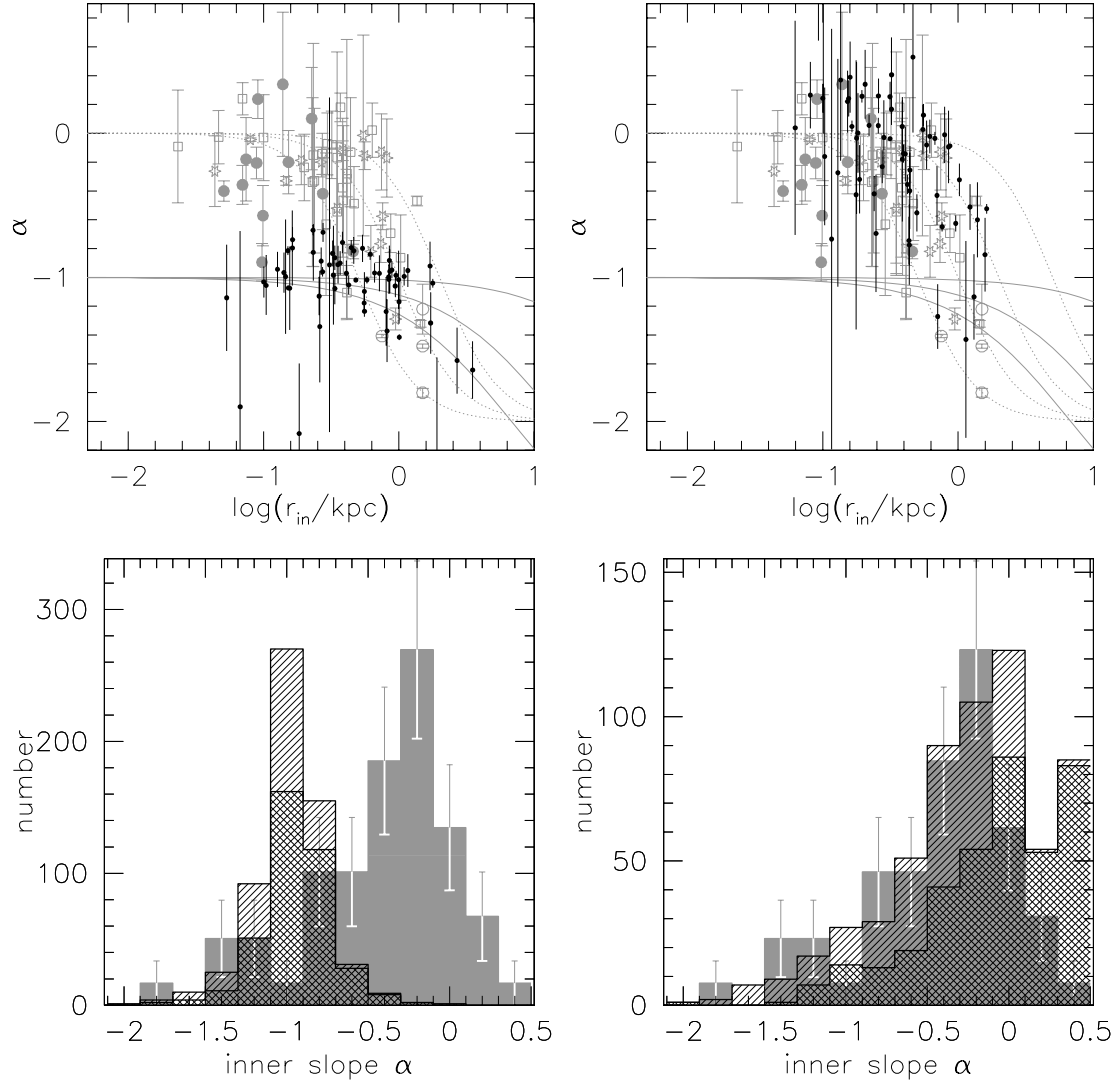


**Figure 8.** Comparison of the simulated NFW (left column) and ISO (right column) haloes with rotation curves modified by small-scale velocity deviations. The top panels compare  $r_{\text{in}}-\alpha$  data points with the observed distribution. The bottom panels show the histograms of  $\alpha$  values for the two models. Apart from extra scatter, the addition of small-scale deviations has not changed the general trend. See Fig. 6.

adding. As well as this softening factor, the number of data points to smooth over were found empirically by demanding that the error bars in the simulated slopes match those of the data. Fig. 8 shows the results. The method has introduced scatter, but not changed the conclusions that were derived from the simulations presented in Fig. 6.

It is clear that the method described above is unsatisfactory. The smoothing and softening factors are arbitrary and ill constrained and the amount of scatter introduced depends strongly on the values we assume for them. Again, the lack of a universally applicable description of what are essentially stochastic and random processes makes this an unfeasible exercise. Furthermore, as the derivation of rotation curves uses extra information such as continuity and symmetry between approaching and receding sides, it is not clear whether the net impact would be significant. Therefore, rather than trying to fine tune a clearly unsatisfactory description we prefer to proceed without it, keeping in mind that there is this missing ingredient, but that it is not likely to affect the conclusions in a significant way.

### 4.3 Lopsidedness and asymmetries

One of the assumptions made in rotation curve analysis is that the velocity field is symmetrical around the dynamical centre. This is not necessarily the case for all galaxies; some seem to have a ‘kinematical lopsidedness’ – see, for example, Swaters et al. (1999) for an extensive description – where the rotation curves of the approaching and receding sides each have different slopes and amplitudes (cf. figure 2 of Swaters et al. 1999). The amplitudes of the curves can differ by up to 20 per cent. Interestingly, kinematical lopsidedness does not seem to automatically imply a spatial offset between optical and dynamical centres. Kinematical lopsidedness can thus affect the interpretation of mass-density slopes.

Here we investigate the effect of kinematical lopsidedness on the rotation curves of NFW and ISO haloes. We model the lopsidedness by computing a rotation curve, but we choose an incorrect point of symmetry (or incorrect systemic velocity). After flipping the rotation curve around this incorrect point of ‘symmetry’, we thus end up

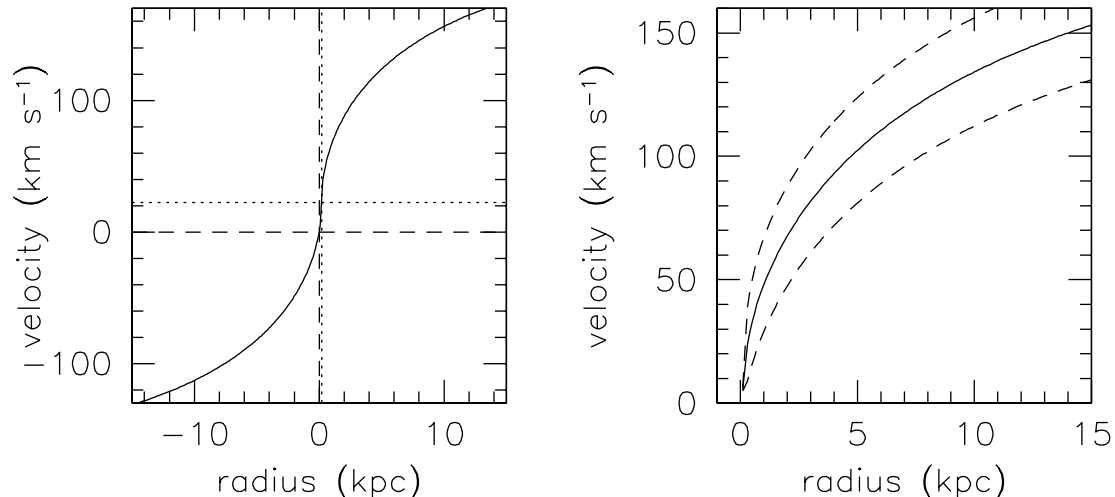


**Figure 9.** Example of the construction of a lopsided rotation curve. The left panel shows a symmetric NFW halo rotation curve. The dotted lines indicate the true point of symmetry, and the dashed lines indicate the ‘wrong’ centre of symmetry used to construct the lopsided curve. The offset is 0.2 kpc in radius and 22 km s<sup>-1</sup> in velocity. The right panel shows the lopsided curve (drawn line) which is the average of the curves of the approaching and receding sides (dashed lines).

with approaching and receding side curves that have different amplitudes and shapes, and therefore different inner slopes. We then proceed to take the average of the inner curves, and determine the mass-density profile.

As the derived slopes are steepest when the point of symmetry is chosen correctly, this procedure will flatten the measured slopes. Fig. 9 shows an example of a ‘kinematically lopsided’ NFW curve. This procedure does not take into account the observed behaviour of the curves at large radii; see, for example, N4395 in Swaters et al. (1999) where one side of the galaxy exhibits a rising rotation curve, while at identical radii on the other side it has already flattened. However, as our interest is in the inner slope, this will not affect any of the conclusions.

We assume offsets of 0.1, 0.5 and 1 kpc. Note that, although the magnitude of the effect is expressed in kpc, we do not imply that this involves a shift in dynamical centre. Our notation is merely a convenient way to express the incorrect choice of systemic velocity that we use to create the kinematical lopsidedness. The offsets used here result on average in velocity offsets of  $\sim 15$ ,  $\sim 30$  and  $\sim 50$  km s<sup>-1</sup>, respectively (see bottom panels in Fig. 10). We also assume that there are no additional offsets between optical and dynamical centres.

Fig. 10 shows the results for the NFW haloes. We see that lopsidedness is not important as long as the effect occurs on scales smaller than the resolution. A lopsidedness of between  $\sim 0.5$  and  $\sim 1$  kpc (which translates into an average velocity shift of  $\sim 40$  km s<sup>-1</sup>) is needed in order to bring most of the NFW points into the  $\alpha = 0$  part of the diagram. The peak at  $\alpha = -1$  in the 0.1-kpc case is caused mainly by well-resolved galaxies. Small offsets are thus inconsistent with NFW models. This peak is still present in the 0.5-kpc case, but is now mainly caused by lower resolution galaxies. The well-resolved galaxies are distributed more like the observed histogram, but with an excess of galaxies with positive slopes. The spread in slopes at these higher resolutions is much larger than observed. Large offsets of  $\sim 1$  kpc are inconsistent with the observed distribution as nearly all well-resolved galaxies exhibit too positive slopes.

The bottom panels in Fig. 10 show the distribution of the velocity differences between approaching and receding sides (not corrected

for inclination) for the various offsets. Also shown is the distribution of the same differences but as a fraction of the halo velocity  $V_{200}$ .

In order to explain the data with NFW models, we thus need to assume a net lopsidedness for *all* galaxies of  $\sim 30$  to  $\sim 60$  km s<sup>-1</sup>. Estimates of the fraction of galaxies that are kinematically lopsided reach up to 30 to 50 per cent (Swaters et al. 1999), but with much smaller velocity differences. It is thus not possible to explain the data with CDM models in combination with lopsidedness alone. We do not show the ISO halo results; ISO haloes already show a slope that is slightly more positive than the data (Fig. 6), and adding in extra flattening due to lopsidedness results in even more positive slopes. ISO haloes are thus not consistent with a large (i.e. shift in symmetry point  $\gtrsim 1$  kpc) kinematical lopsidedness.

#### 4.4 Non-circular motions

A frequently-made assumption is that the visible matter in a galaxy is on circular orbits, and therefore that the measured line-of-sight velocities represent the true rotation velocity. If, however, part of the measured velocity is due to non-circular motions, it is no longer a representative indicator of the mass content of a galaxy. Systematic non-circular motions are most commonly observed as streaming motions along bars or spiral arms (we do not consider local non-circular motions due to, for example, star formation or supernovae, as explained in Sections 3.3 and 4.2). Bright galaxies can show large streaming motions; e.g.  $\sim 30$  km s<sup>-1</sup> in M81 (Adler & Westpfahl 1996) or  $\sim 20$  km s<sup>-1</sup> in NGC 1365 (Jörsäter & van Moorsel 1995). These galaxies are, however, mostly grand-design spirals with pronounced spiral structures. Streaming motions in late-type spirals such as M33, NGC 300, 925 or 1744 are found to be much smaller, and barely distinguishable from random motions in the disc (i.e.  $\lesssim 10$  km s<sup>-1</sup>) (Deul & van der Hulst 1987; Puche, Carignan & Bosma 1990; Pisano et al. 1998). LSB galaxies are similar to these late-type galaxies and would not be expected to have large circular motions. H I velocity fields also show no evidence for large systematic non-circular motions  $\gtrsim 10$  km s<sup>-1</sup> (de Blok et al. 1996; Woldrake, de Blok, Walter 2003).

We model non-circular streaming motions by introducing a radial velocity component (see equation 1). The effects of streaming motions on a rotation curve are strongest when they are oriented

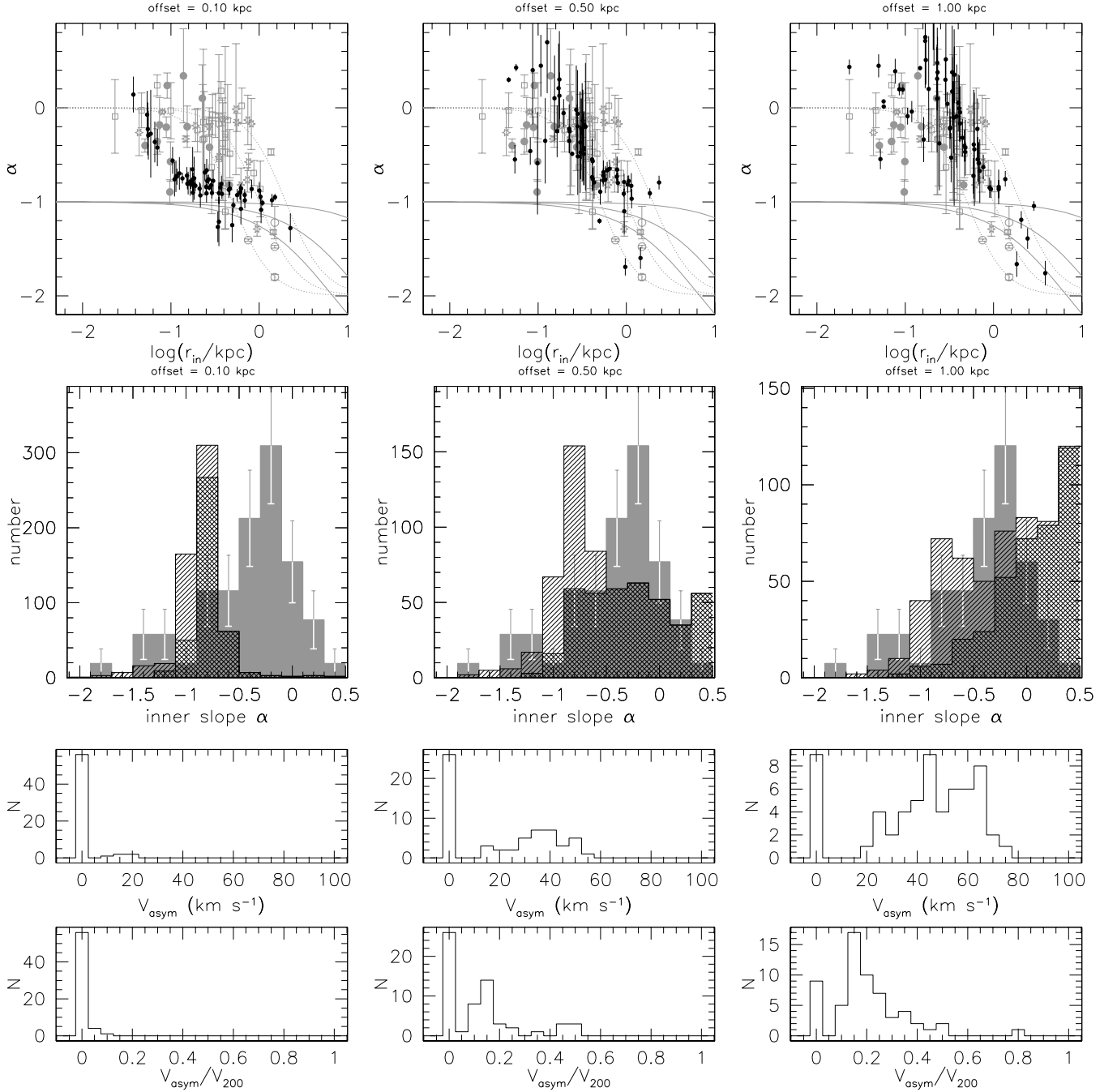


**Figure 10.** As Fig. 6, but now showing the results for NFW haloes in combination with kinematical lopsidedness of 0.1 kpc (left column), 0.5 kpc (centre column) and 1 kpc (right column). The bin at  $\alpha = 0.5$  also contains galaxies with  $\alpha > 0.5$ . The bottom panels show the distribution of the resulting velocity differences between approaching and receding sides, both in absolute terms, and as a fraction of halo rotation velocity  $V_{200}$ . The peak at  $V = 0$  is due to galaxies at large distance or low inclinations where the kinematical lopsidedness shift is much less than one resolution element.

parallel to the minor axis. We approximate this by adding a constant velocity component to the rotation curve over the inner one-third of its radius (the exact range is not important as we use only the inner points to determine the mass-density profile). We thus use equation (1) but change the phase of the radial component by  $\pi/2$ . Again we only show the results for the NFW haloes, as the ISO haloes are only consistent with no or very small non-circular motions, for the same reason as with kinematical lopsidedness; their profiles are already slightly flatter than the data, and more flattening is not needed.

We have computed models for streaming velocities of 5, 10 and 20  $\text{km s}^{-1}$ . Fig. 11 shows that systematic streaming motions of the order of  $\sim 20 \text{ km s}^{-1}$  are needed to at least partially explain the data for the well-resolved galaxies with a NFW halo. There is, however, still an excess of data points with slope  $\alpha = -1$  formed of low-resolution galaxies, as well as an excess of positive slopes due to well-resolved galaxies. The bottom panels in Fig. 11 show that, for a significant fraction of the galaxies, a streaming motion of this magnitude amounts to  $\sim 20$  per cent or more of the halo velocity  $V_{200}$ . In order to use streaming motions in combination with NFW

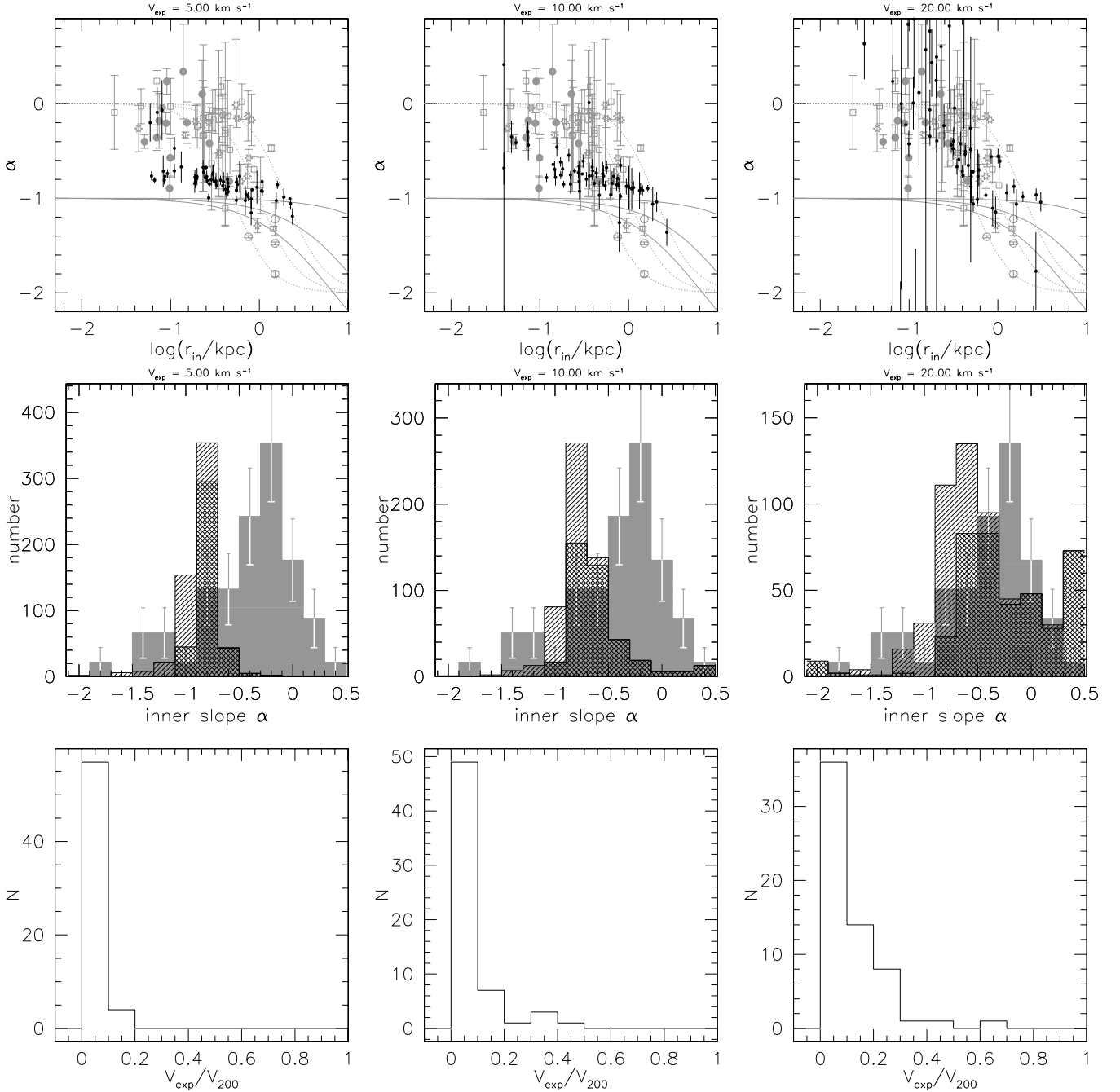


**Figure 11.** As Fig. 6, but now showing the results for NFW haloes in combination with streaming motions parallel to the minor axis. The left column shows results for  $5 \text{ km s}^{-1}$ , the centre column results for  $10 \text{ km s}^{-1}$  and the right column results for  $20 \text{ km s}^{-1}$ . The bin at  $\alpha = 0.5$  also contains galaxies with  $\alpha > 0.5$ . The bottom panels show the distribution of the magnitude of the streaming motion as a fraction of the halo velocity  $V_{200}$ .

haloes, we thus need to assume that *all* galaxies have systematic non-circular motions over a large part of the disc of the order of  $\sim 20 \text{ km s}^{-1}$ . This contradicts the observational data for late-type galaxies.

#### 4.5 Mismatched position angles

A mismatch between the true PA and the observed PA does not lead to a change in slope for axisymmetric potentials. As can be seen from equation (1) it will merely introduce a scale factor of order  $\cos \theta / \cos$

$\theta'$  where  $\theta$  and  $\theta'$  are the true PA and mismatched PA, respectively. In the absence of non-circular motions and in axisymmetric potentials we can even correct for a mismatched PA. If the mass distribution in the central parts is not axisymmetric, then the precise value of the PA becomes important. However, in these cases the inner parts of the galaxy are likely to be dominated by the stellar component, or the halo is very triaxial. In these cases the minimum disc and spherical halo assumptions are no longer valid. We need to make self-consistent multi-component galaxy models, and can no longer use the simple one-component models we have been using.

#### 4.6 Offsets between dynamical and optical centres

It is generally assumed that in a galaxy the optical centre and the dynamical centre coincide. However, if this is not the case, then, at least for NFW haloes, measuring the kinematics around the optical centre will lead to the impression that the slope of the inner mass-density profile is shallow rather than steep.

It is known that in some late-type (barred) galaxies the optical centre can be located up to  $\sim 1.5$  kpc away from the dynamical centre (Pisano et al. 1998; de Vaucouleurs & Freeman 1972; Weldrake et al. 2003). This ‘morphological lopsidedness’ is different from the kinematical lopsidedness discussed before, in that as long as the stellar population is unimportant, the potential can still be dominated by the halo and be axisymmetric around the dynamical centre. It should be stressed though that, for the majority of bright galaxies where the kinematics have been investigated in detail, the optical centre and dynamical centre do coincide (cf. Begeman 1987). In these galaxies the slit would sample the true dynamical centre.

To model the effect of offsets between dynamical and (observed) optical centres, we run the simulations assuming a distribution of offsets and we observe the haloes with a slit offset from the dynamical centre (see Fig. 2). We assume Gaussian distributions of offsets with dispersions  $\sigma = (0.5, 1, 2, 3, 4, 5, 6)$  arcsec. For each of these seven cases we run the simulations twice, once producing 600 NFW haloes and once producing 600 ISO haloes. As an offset between the dynamical and optical centres is equivalent to a slit offset, we draw a random slit offset from the relevant Gaussian offset distribution for each halo (i.e. the first case produces 600 NFW and 600 ISO haloes, each observed with offset slits, where the distribution of slit offsets was Gaussian with a dispersion  $\sigma = 0.5$  arcsec, and so on for all other values of the dispersion). We have also modelled uniform distributions using widths identical to the dispersions listed above, with identical conclusions as the Gaussian distributions.

##### 4.6.1 NFW haloes

In Fig. 12 a random selection of 10 rotation curves derived assuming a Gaussian offset distribution with  $\sigma = 5$  arcsec is shown in comparison with the corresponding no-offset rotation curves. Also shown are the corresponding mass-density profiles. For the average distance of the observed sample of  $\sim 73$  Mpc, this dispersion corresponds to a physical dispersion of  $\sim 1.8$  kpc. We use such a large offset dispersion to clearly show the differences between the curves, which would hardly be visible for smaller dispersions.

The  $r_{\text{in}}-\alpha$  comparison is shown in Fig. 13. The observed and theoretical distributions are distinctly different, as also seen in the histograms in Fig. 14. The NFW models show a pronounced peak at  $\alpha = -1$  not seen in the data. The high-resolution and low-resolution histograms look very similar. The only way to explain the observed distribution with NFW haloes and centre offsets is to assume that for all galaxies observed the position of the dynamical centre is offset from the optical centre by  $\sigma \sim 3-4$  arcsec. At higher dispersions the distributions becomes too biased towards  $\alpha = 0$ . We can put this in context by comparing with the average scalelength of the F-LSB galaxies in de Blok, van der Hulst & Bothun (1995), which is 11 arcsec. Compared to the sizes of the optical discs, the offsets needed are thus significant. Similar conclusions can be derived for uniform offset distributions.

##### 4.6.2 ISO haloes

In Fig. 15 a random selection of 10 rotation curves derived assuming the ISO model and a Gaussian offset distribution with  $\sigma =$

2 arcsec is shown in comparison with the corresponding no-offset rotation curve. Also shown are the corresponding mass-density profiles. The  $r_{\text{in}}-\alpha$  plots and histograms for the ISO model are presented in Fig. 16. The ISO simulations are a better (although not perfect) match to the data than the NFW simulations. ISO haloes are fairly insensitive to the effects of moderate offsets between optical and dynamical centres. We thus only present the results  $\sigma < 2$  arcsec.

The peak in the simulated distribution occurs at  $\alpha = 0$ , offset from the observed  $\alpha = -0.2 \pm 0.2$ . There is an excess of steeper slope galaxies in the observations. The inner parts of real galaxies clearly have density profiles that are not precisely flat. A possible explanation is that the minimum-disc assumption is slightly inappropriate, and that the stellar disc causes the steeper observed slopes. However, as stated before, modelling this effect is beyond the scope of our simple one-component models. The values of the slopes are insensitive to the precise value of the offset, indicating that if galaxies do have ISO haloes, they will always be obvious from the observations. The simplest explanation is that offsets between optical and dynamical centres are small.

##### 4.6.3 Observational offsets

A mismatch between the centres has the same effect as an incorrectly centred slit. The absence of systematic differences thus also implies an absence of these observational offsets. This is to be expected from a technical point of view; the optical centres in LSB galaxies are often visible in the slit camera, and in most cases used to line up the slit of the spectrograph with the galaxy. The accuracy of a typical telescope pointing system and the accuracy of the offset procedure from nearby stars is generally very good. Offset and pointing tests performed during the observations generally are repeatable down to the  $\sim 0.3$  arcsec level. This has already been addressed by McGaugh et al. (2001) and dBB02, who have presented rotation curves of a few LSB galaxies that have been observed multiple times at different dates on different telescopes by different observers. It is shown that these agree very well with each other; see also Marchesini et al. (2002). Residual observational uncertainties could be introduced by the process of measuring the positions of the centres of the galaxies from, for example, CCD images, catalogues or H I observations. These offsets can, for obvious reasons, only be a small fraction of the size of the galaxy, and are therefore  $\sim 1$  arcsec or less, consistent with the scatter implied by the simulations.

## 5 TESTS WITH REAL DATA

To test whether some of the effects described above are observable in practice, we re-observed one of the galaxies from dBB02. We chose UGC 4325, which is a typical late-type dwarf galaxy. It is nearby ( $D = 10.1$  Mpc), resulting in a linear resolution of  $\sim 50$  pc arcsec $^{-1}$ . Its H I velocity field is regular, symmetric and appears undisturbed (Swaters 1999) with an inclination of  $41^\circ$ .

UGC 4325 was observed in early 2002 February with the 1.93-m telescope at the Observatoire de Haute Provence using the long-slit Carelec spectrograph. The set up, observing procedures and data reduction were identical to those described in dBB02. We obtained H $\alpha$  spectra of UGC 4325 along its major axis (PA  $231^\circ$ ), parallel to the major axis but offset by  $+5$  arcsec (0.25 kpc), parallel to the major axis offset by  $-5$  arcsec, as well as two spectra centred on the galaxy but with PA offsets of  $+30^\circ$  and  $-30^\circ$ .

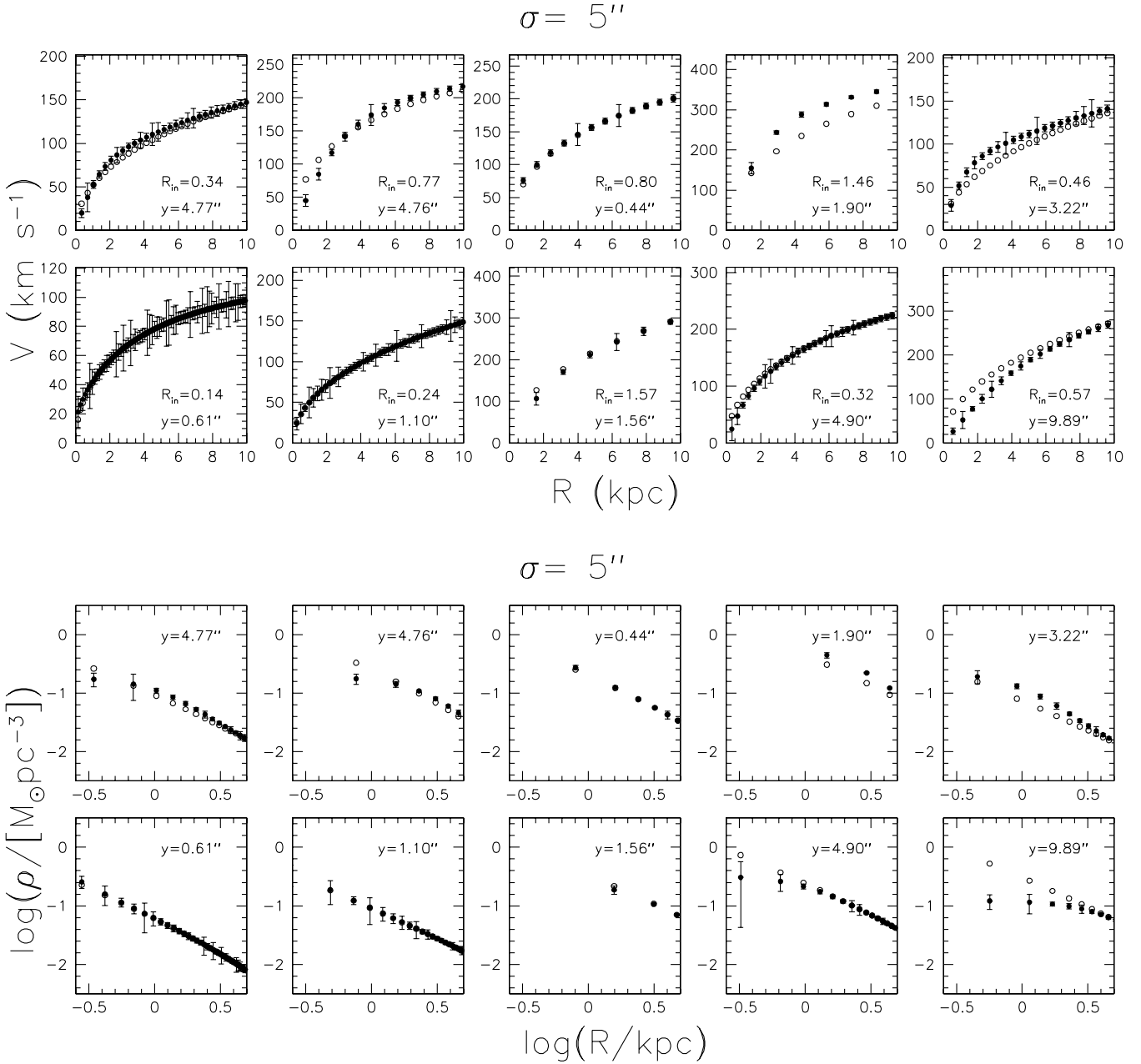


**Figure 12.** A random selection of simulated NFW rotation curves (top panels) and corresponding density profiles (bottom panels). The open circles show the original major-axis curves and profiles, while the filled circles with error bars show the off-axis curves and profiles. A Gaussian scatter with  $\sigma = 5$  arcsec was used for these curves. The actual value is given at the top of each panel, along with the resolution (separation between points) in kpc.

The resulting raw rotation curves (not corrected for inclination) are shown in the top row of Fig. 17. Especially for the offset curves, the positions of the ‘centres’ along the slit are difficult to determine, and we determined the systemic velocity and central position by looking for the point that gave maximum symmetry between approaching and receding sides. However, as the curves are almost linearly rising in the inner parts, the precise choice of the centre of symmetry does not affect the slopes. The symmetrized and uncorrected curves are shown in the second row of Fig. 17. Following de Blok et al. (2001a), we have performed local polynomial fits to the folded curves in order to bring out the underlying shape. We also re-sampled the curves with a spacing of 4 arcsec. The resulting curves

are shown in the third row of Fig. 17. Also shown in the bottom row are the mass-density profiles.

The similarity between the major-axis curve and the two off-axis curves is more consistent with an ISO model and velocity field as shown in Fig. 3. The curves with PA offsets only show modest changes in the slope, consistent with U4325 having a fairly axisymmetric potential, and negligible streaming motions. For UGC 4325 the systematic effects discussed in this paper are not obviously present and are likely small enough to be unobservable. If UGC 4325 is typical, then the data presented here show that the systematic effects discussed in Section 3 are unlikely to have a large effect on the observed rotation curves.

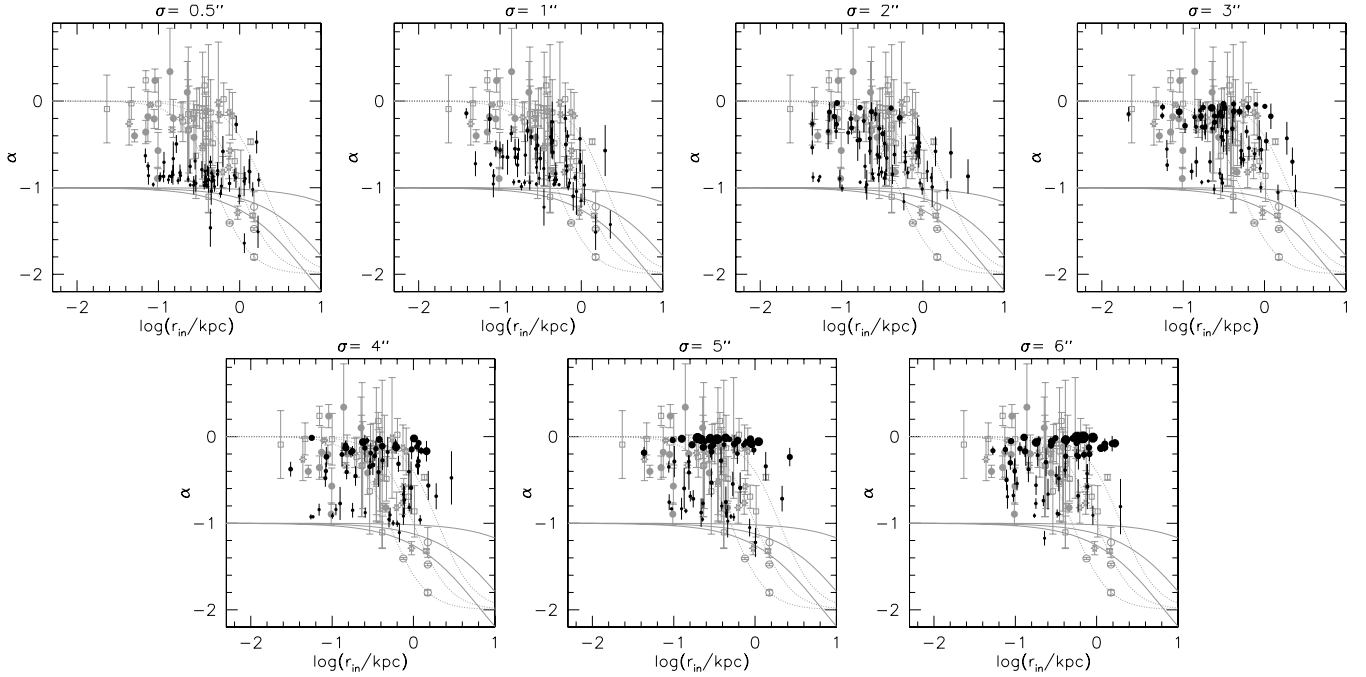


**Figure 13.** Comparison of the simulated NFW halo  $r_{in}$ - $\alpha$  data points with the observed distribution. The simulated data points were derived using random centre offsets, where the offsets have a Gaussian distribution with the dispersion given above each panel. As in Fig. 6.

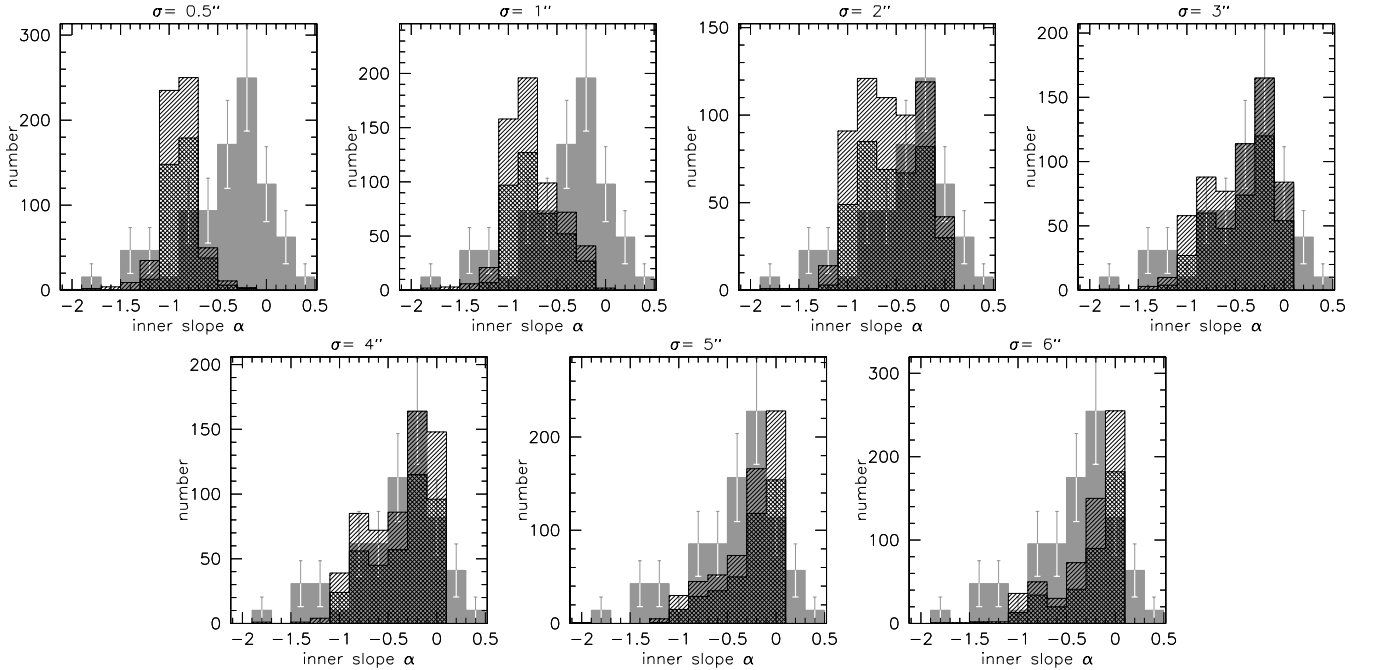


**Figure 14.** Comparison of the simulated distribution of the slopes of NFW haloes (hatched histogram) – low-resolution galaxies (single-hatched) and high-resolution galaxies (cross-hatched) – with that actually observed (grey histogram). The dispersion of the Gaussian distribution for offsets is given above each panel.

## 6 DISCUSSION

If systematic effects indeed play only a small role in determining the observed mass-density profile, some of the scatter in the observed value of the slope could be due to intrinsic differences in the shapes of the mass-density profiles. This can be used to improve on the

results for the ISO halo. Fig. 16 shows that for this model the peak in the histogram occurs at values of  $\alpha$  that are slightly too large. Here we discuss two additional observationally motivated models that were designed as an improvement on the ISO model: the first is the halo of Burkert (1995) (Section 6.1); the second is the halo

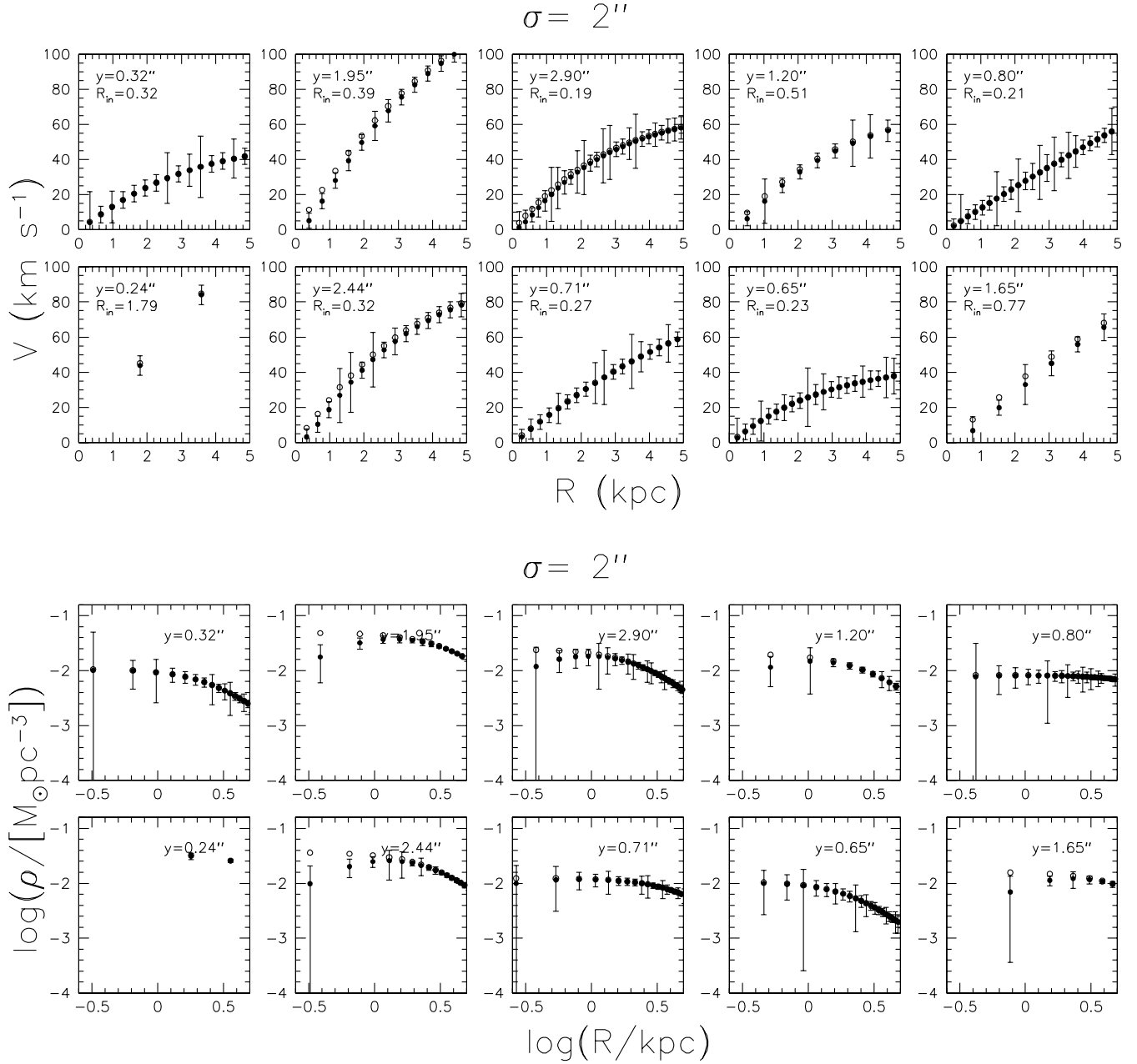


**Figure 15.** As Fig. 12, but showing ISO curves and profiles.

model proposed by Kravtsov et al. (1998) based on LSB HI rotation curves (Section 6.2).

### 6.1 Burkert haloes

The halo model presented in Burkert (1995) is a compromise between the ISO and CDM models; it has the constant density core found in ISO haloes, but shows the steep drop-off in density at large radii found in CDM simulations. The density profile of a Burkert halo can be described as

$$\rho(R) = \frac{\rho_0}{(1 + R/r_0)(1 + (R/r_0)^2)} \quad (11)$$

and the corresponding rotation curve is given by

$$V^2(R) = 2\pi G \rho_0 r_0^3 \frac{1}{R} \times \left\{ \ln \left[ \left( 1 + \frac{R}{r_0} \right) \sqrt{1 + \left( \frac{R}{r_0} \right)^2} \right] - \arctan \frac{R}{r_0} \right\}, \quad (12)$$

where  $r_0$  is the equivalent of a core radius and  $\rho_0$  is the central density. This particular model gives a good description of the rotation curves of dwarf and LSB galaxies (Burkert 1995; Blais-Ouellette et al. 2001; Marchesini et al. 2002). However, the steep  $R^{-3}$  drop-off in density in the outer parts, as implied by the above equations, has not been observed unambiguously, and therefore fits using this model mostly constrain the inner part of the curve. Here we characterize the Burkert halo in terms of its maximum rotation velocity,

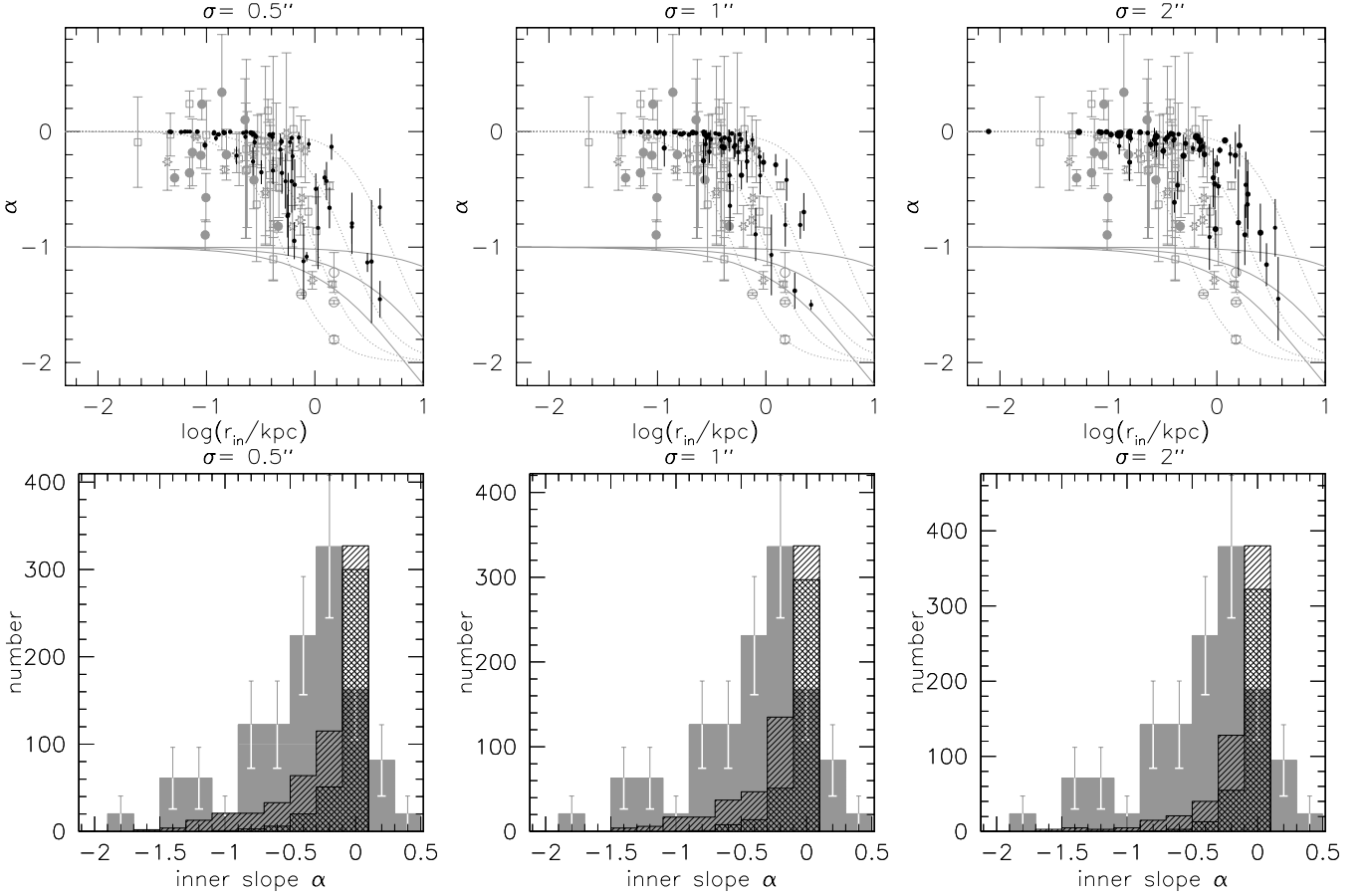


**Figure 16.** As Figs 13 and 14, but now showing the results for ISO haloes. The bin at  $\alpha = 0.5$  also contains galaxies with  $\alpha > 0.5$ .

making the assumption that the observed rotation curves do not probe the declining  $\rho \sim R^{-3}$  part of the rotation curve.  $V_{\max}$  occurs at  $R_{\max} = 3.25 r_0$ , and we can express  $r_0$  as

$$r_0 = \sqrt{\frac{V_{\max}^2}{0.8606\pi G \rho_0}}. \quad (13)$$

We describe the selection of halo parameters for the simulated Burkert haloes in Section 6.3.

## 6.2 Kravtsov haloes

The distribution of observed inner mass-density slopes peaks at a value of  $\alpha = -0.2$  (dMBMR, dBB02). Before the optical rotation curves used in those analyses became available, Kravtsov et al. (1998) fitted power-law models to the H I rotation curves of dwarf and LSB galaxies; the latter from de Blok et al. (1996). They found that the inner rotation curves could be described with a power law with a slope  $\alpha_{\text{HI}} = -0.2$ . (The agreement between the optical and H I values is certainly an indication that the effects of beam smearing on the majority of the H I curves must have been minor.)

The density profiles described so far are part of a wider set of profiles of the form (Kravtsov et al. 1998; Zhao 1996; Blais-Ouellette et al. 2001)

$$\rho(R) = \frac{\rho_0}{[q + (R/r_0)^{-a}] [1 + (R/r_0)^\gamma]^{(\beta+\alpha)/\gamma}} \quad (14)$$

where we have changed the order and signs of some of the exponents as defined in Kravtsov et al. (1998) and Blais-Ouellette et al. (2001)

to be consistent with our notation. The above equation can be used to describe NFW haloes with  $(q, \alpha, \beta, \gamma) = (0, -1, 3, 1)$ , ISO haloes with  $(1, -2, 2, 2)$  while the Burkert halo has the parameter set  $(1, -1, 3, 2)$ . The parameter  $\alpha$  determines the inner slope,  $\gamma$  determines the rate of turnover in the mass profile, while  $\beta$  gives the slope of the mass distribution in the outer parts of haloes. The  $q$  parameter indicates the presence ( $q = 1$ ) or absence ( $q = 0$ ) of a constant-density core. Kravtsov et al. (1998) have found that the LSB H I rotation curves from de Blok et al. (1996) can be best described with the parameter set  $(0, -0.2, 3, 1.5)$ . They have noted that the  $\gamma$  and  $\beta$  parameters are difficult to constrain and have chosen values suggested by CDM simulations. Although we use these values, we note that the observed mass profiles of LSB galaxies are equally well described by asymptotically flat rotation curves with  $\beta = 2$ . As we are here only interested in the inner parts of the haloes, this choice does not affect the results.

The corresponding rotation curve can be described by a model of the form

$$V(R) = V_t \frac{(R/r_0)^g}{[1 + (R/r_0)^a]^{(g+b)/a}}. \quad (15)$$

The parameter  $g$  gives the inner slope of the rotation curve and is related to  $\alpha$  by  $g = 1 + \alpha/2$  (note our definition as  $\alpha$  as a negative number). We thus find  $(a, b, g) = (1.5, 0.34, 0.9)$ . The maximum rotation velocity is related to  $V_t$  by  $V_{\max} = V_t (g/a)^{g/a} (1 + g/b)^{-(b+g)/a}$ . The parameter sets  $(q, \alpha, \beta, \gamma) = (0, -0.2, 3, 2)$  and  $(a, b, g) = (1.5, 0.34, 0.9)$  thus fully describe the mass-density profiles and rotation curves of a halo with an  $\alpha = -0.2$  inner mass-density

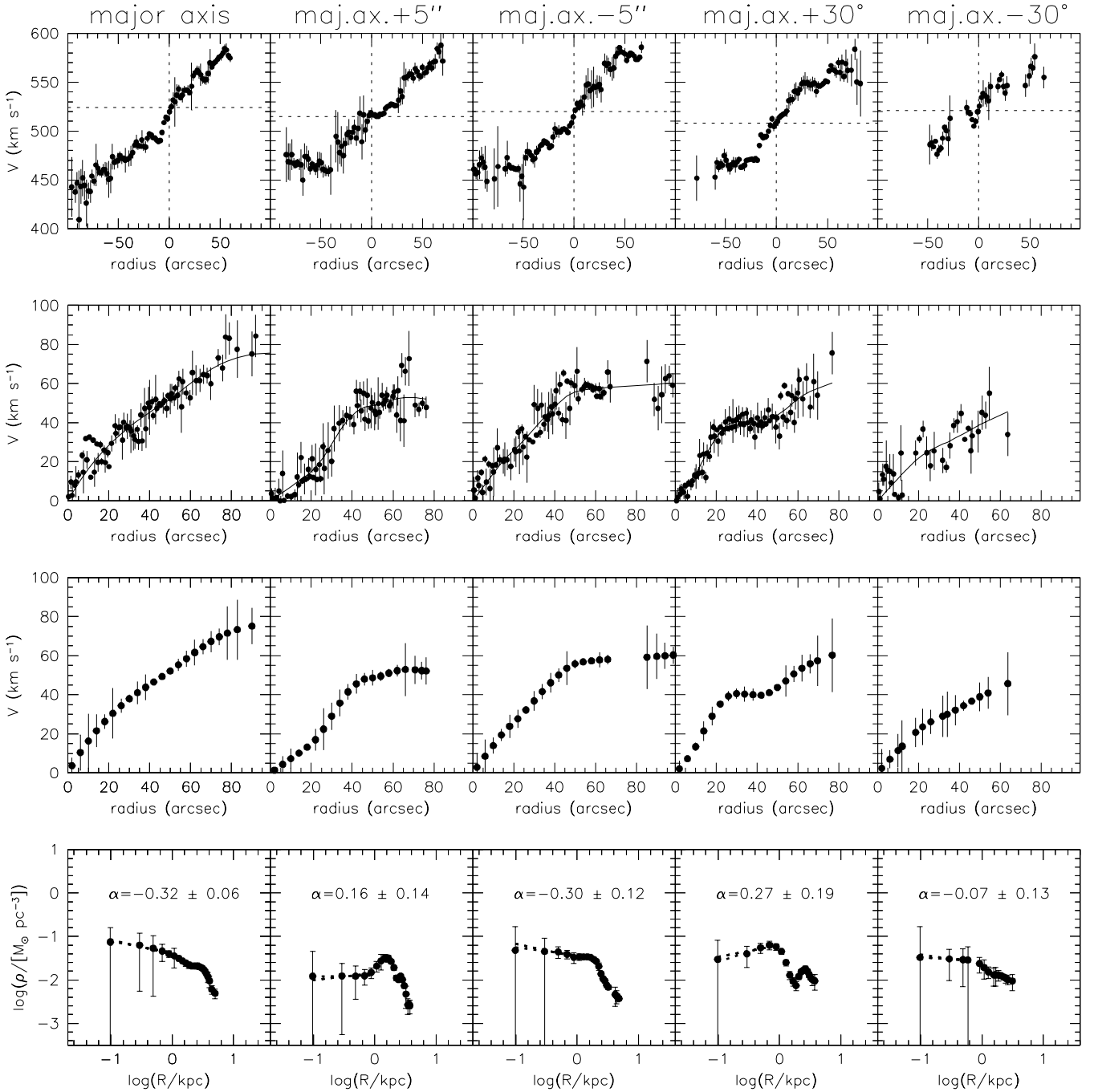


**Figure 17.** Observed rotation curves of UGC 4325, after applying spatial and PA offsets. From left to right: major-axis rotation curve; parallel to major-axis offset by +5 arcsec; parallel to major-axis offset by −5 arcsec; PA offset of +30°; PA offset of −30°. The top row shows the raw rotation curves, the second row shows folded rotation curves, the third row shows re-sampled rotation curves, and the bottom row shows mass-density profiles derived from the re-sampled rotation curves.

profile. These profiles will be used to optimize the description of the data by our simulations.

### 6.3 Scaling the models

The NFW and ISO models each have a well-defined range of allowed halo parameters, either derived from cosmological simulations or observations. These ranges are less well defined for the

Burkert and Kravtsov haloes. In order to simulate these haloes with realistic parameters we assume that the ISO curves modelled here are a good description of observed rotation curves. We scale the Burkert and Kravtsov models to show the same diversity in shapes and amplitudes.

The left panel in Fig. 18 compares the rotation curves of each of the three models for  $V_\infty = V_{\max} = V_t = 100 \text{ km s}^{-1}$ , and  $R_C = r_0 = 1 \text{ kpc}$ . Using these identical numerical parameters the

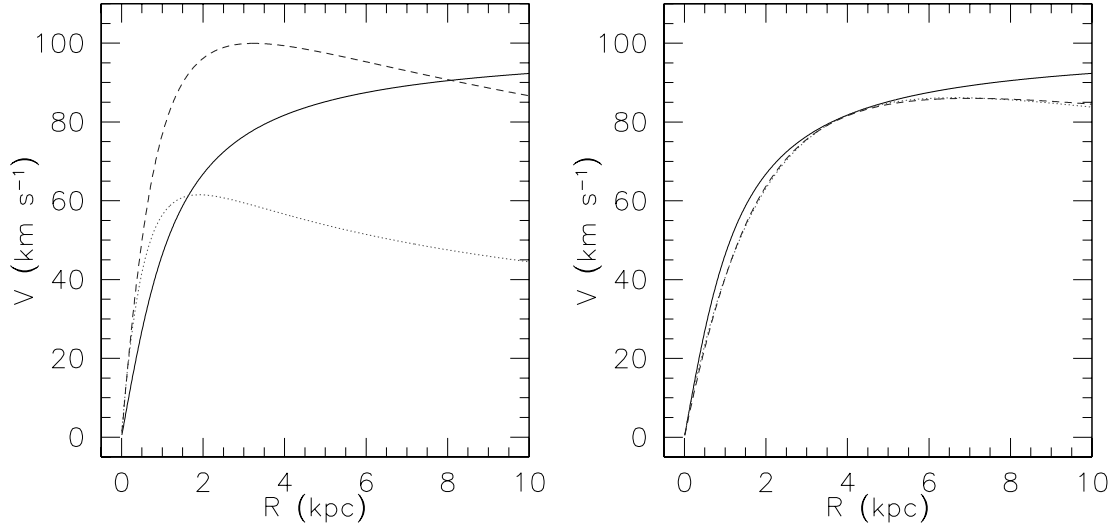


**Figure 18.** Comparison of the rotation curves of the ISO, Burkert and Kravtsov models, before and after scaling. The left panel shows rotation curves of the three models, assuming  $V_\infty = V_{\max} = 100 \text{ km s}^{-1}$  and  $R_C = r_0 = 1 \text{ kpc}$ : full drawn curve, ISO halo; dotted curve, Kravtsov halo; dashed curve, Burkert halo. The right panel shows the three curves after the scaling described in the text.

ISO curve rises more slowly than the Burkert and Kravtsov curves. The latter has a lower maximum velocity, as for this model  $V_{\max} = 0.62 V_t$  (see Section 6.2). Simply using identical halo parameters in the simulations thus makes the Burkert and Kravtsov haloes consistently more compact and more likely to suffer from systematic resolution effects. The differences in Fig. 18 are due to the different scalings that  $r_0$  and  $R_C$  imply in the various models and we can scale the curves in order to obtain a more consistent behaviour. Equations (10) and (13) show that, for a given central density and maximum or asymptotic velocity, the ISO and Burkert radii scale as  $R_C/r_0 = 1/2.156$ . For a given central density and maximum velocity, we need to assume a value of  $r_0$  that is  $\sim 2.2$  times larger than the corresponding value of  $R_C$  in order to obtain a Burkert curve that matches approximately the shape of the ISO curve. The Burkert and Kravtsov curves can be scaled in radius by considering their maximum rotation velocities. For the Burkert halo this occurs

at  $r = 3.25 r_0$ ; for the Kravtsov halo at  $r = 1.91 r_0$ . A scaling of 1.69 in radius will thus line up the Kravtsov curve with the Burkert curve (which implies a total scaling of 3.64 with respect to the ISO halo).

The velocity scales can be matched with those of the ISO haloes by multiplying the velocities of the Burkert halo by 0.86; that of the Kravtsov halo by multiplying by 1.38. We do not normalize to the asymptotic velocity of the ISO halo as might perhaps be expected, as this would have resulted in substantially different shapes. The right panel in Fig. 18 shows the scaled rotation curves. This procedure thus merely serves to provide a sample of simulated Burkert and Kravtsov curves with shapes that match those shown by the ISO curves (and as observed in real galaxies). This minimizes possible systematic effects in the simulations due to differences in shape or resolution. The scaling does not affect the values of the central slopes.

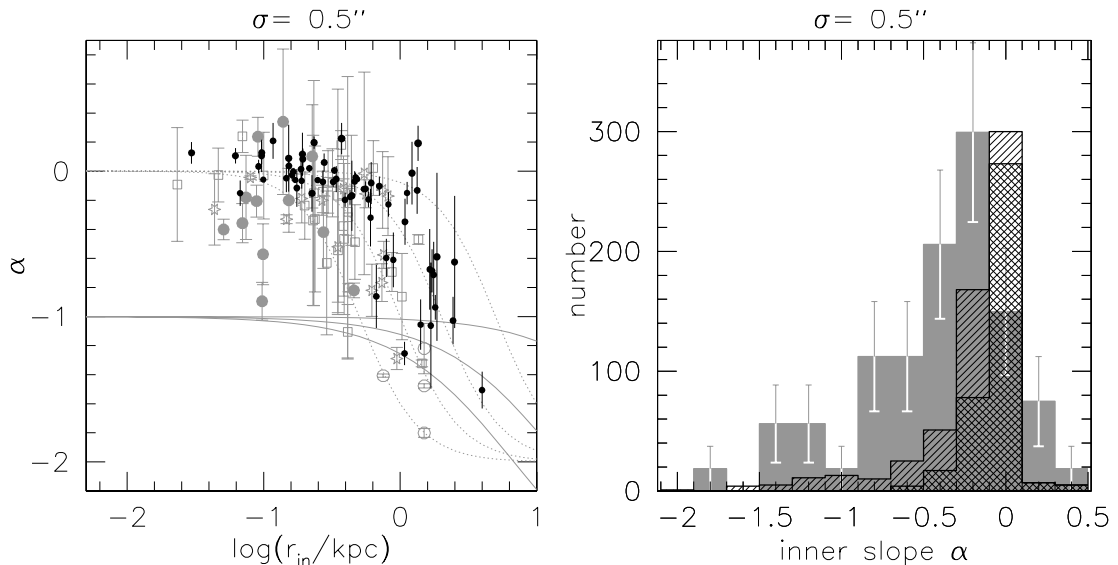


**Figure 19.** As Figs 13 and 14, but now showing the results for Burkert haloes. The bin at  $\alpha = 0.5$  also contains galaxies with  $\alpha > 0.5$ .

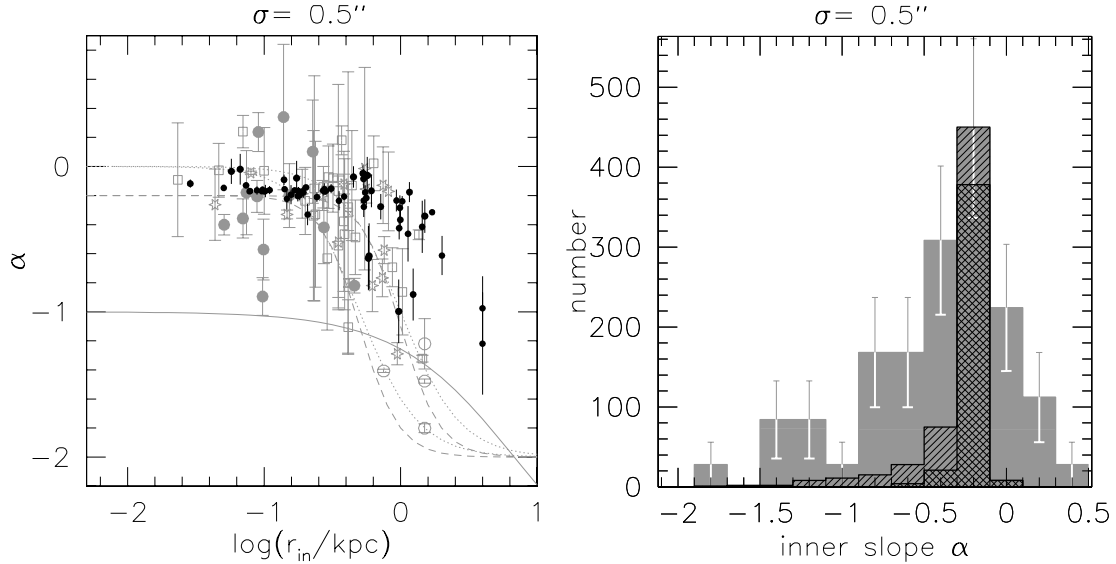


**Figure 20.** As Figs 13 and 14, but now showing the results for Kravtsov haloes. The bin at  $\alpha = 0.5$  also contains galaxies with  $\alpha > 0.5$ .

In order to simulate a realistic range of parameters for the Burkert and Kravtsov haloes we sample the same numerical range of parameters as for the ISO haloes (as described in Section 3.2.2), and we multiply their radial and velocity scales by the factors described above.

#### 6.4 Results for Burkert and Kravtsov haloes

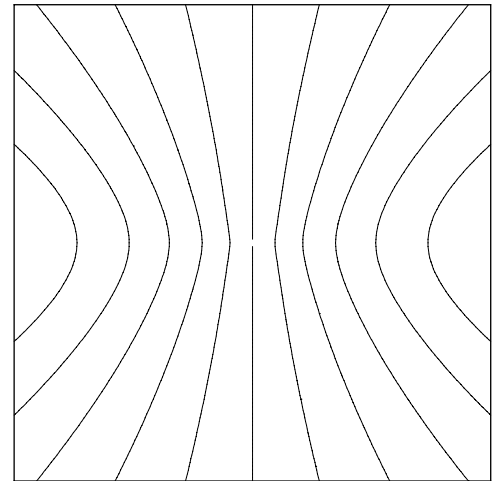
As we have established that the systematic effects for core-dominated models can only be small, we concentrate here on the simulation results in the absence of these effects, except for the small  $\sigma = 0.5$  arcsec scatter in the position of the dynamical centre (see Section 4.6.2). Results for the Burkert haloes are expected to be similar to those of the ISO model, as the Burkert model was designed to be a compromise between a core model in the inner parts and a CDM  $\rho \sim R^{-3}$  model in the outer parts. As is clear from Fig. 19, the only real difference is that the Burkert models show a slightly larger number of steep slopes than the ISO model, due to the steeper drop-off in the outer parts.

Fig. 20 shows the results for the Kravtsov haloes. The peak of the histogram distribution now matches well (but was constructed to do so). The  $r_{\text{in}}-\alpha$  distributions show slopes that are slightly too shallow for large values of  $r_{\text{in}}$ . This is introduced by the rotation curve scaling we used and the points can be shifted horizontally by using a different scaling. However, as we are only interested in the global trends, and are not trying to model individual galaxies in detail, we retain our simple scaling relations. The scaling does not affect the inner slopes.

We show the velocity field of a Kravtsov halo in Fig. 21. The halo parameters were chosen to give a rotation curve similar to that used for the ISO velocity field in Fig. 3. The shapes of the iso-velocity contours are very similar to the ISO velocity field, and do not show the ‘pinching’ that the NFW iso-velocity contours show.

#### 6.5 Kravtsov haloes with scatter

The Kravtsov model fits the peak in the  $\alpha$  histogram best, but was of course constructed to do so. One feature of the data that none of



**Figure 21.** Velocity fields of the inner parts of massless discs embedded in a Kravtsov halo. The velocity field is seen under an inclination angle of  $60^\circ$ , and a PA of  $90^\circ$ . The boxes measure  $5 \times 5 \text{ kpc}^2$ . The vertical minor-axis contour is  $0 \text{ km s}^{-1}$ , increasing in steps of  $10 \text{ km s}^{-1}$  outwards. The halo parameters are  $r_0 = 3.64 \text{ kpc}$  and  $V_{\text{max}} = 138 \text{ km s}^{-1}$ .

the three core-dominated models can reproduce is the wings towards steeper slopes found in the data histogram. It is easy to produce shallower slopes with systematic effects, but very few effects actually will produce steeper slopes. Furthermore, the ‘monolithic’ nature of the models (for each model all haloes have identical slopes) creates pronounced peaks in the histograms. In real galaxies we might expect the contributions of, for example, the disc to differ from galaxy to galaxy, introducing a scatter in the values for the inner total mass-density slope. We test here the hypothesis that there is a small scatter in the intrinsic value of the inner slopes which is responsible for the observed wings in the data histograms.

We use the Kravtsov model and add a small Gaussian scatter to the slope. We choose an intrinsic dispersion in the mass-density slope  $\sigma_\alpha = 0.2$ . This choice has no physical motivation, but is simply suggested by the width of the peak in the data histogram. Other

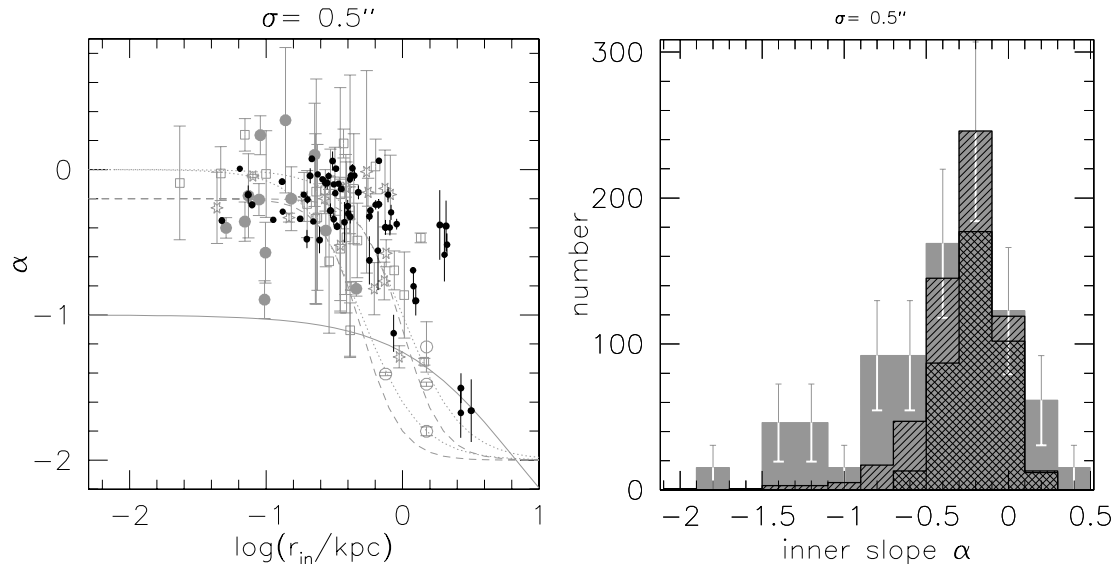


**Figure 22.** As Figs 13 and 14, but now showing the results for Kravtsov haloes with a  $\sigma_\alpha = 0.2$  Gaussian scatter added to the value for the inner slope. The bin at  $\alpha = 0.5$  also contains galaxies with  $\alpha > 0.5$ .

more fine-tuned choices may very well be possible; our aim here is simply to describe the data in as few assumptions as possible with a simple one-component model. Adding a Gaussian scatter  $\sigma_\alpha$  to the  $\alpha$ -parameter in equation (14), implies modifying the  $g$ -parameter in equation (15) with a Gaussian contribution with dispersion  $\sigma_g = \sigma_\alpha/2$ .

The results for the Kravtsov simulations with scatter  $\sigma_\alpha = 0.2$  are shown in Fig. 22. The peak again matches (naturally). The high- and low- $\alpha$  wings of the histogram fit the data better than previous models. The value for the scatter can probably be fine tuned, and the distribution of the scatter is most likely not Gaussian (our assumptions in a small number of cases lead to hollow haloes). The observed distribution of slopes is thus consistent with haloes with inner slopes  $\alpha = -0.2 \pm 0.2$  ( $1\sigma$ ) and no systematic effects.

## 7 CONCLUSIONS

We have investigated the effect of systematic effects such as non-circular motions, asymmetries and lopsidedness on the values of the inner slopes of various halo models. We find that no realistic combination of a single systematic effect and NFW models can explain the observed distribution of slopes.

Core-dominated models, on the other hand, are consistent with the data in the absence of large systematic effects. The best match to the data is obtained by using haloes with an inner mass-density slope  $\alpha = -0.2$  and an intrinsic Gaussian scatter in the slope of  $\sigma_\alpha \sim 0.2$ . As our models assume minimum disc, these slopes should be interpreted as those of the combined mass profiles of stars, gas and dark matter in a galaxy.

It is perhaps possible to construct a combination of multiple systematic effects to explain the data in the CDM framework. However, such a combination of effects would have to completely wipe out the strong  $\alpha = -1$  peak in the  $\alpha$  histograms. The resulting models would be completely dominated by non-cosmological effects, and not contain any link between properties of dark matter haloes and the visible galaxies that inhabit them. Yet, they would have to explain and obey the Tully–Fisher relation, for example, and thus require a tremendous amount of fine tuning.

The implied observational signature of CDM haloes is strong and, if present, should be easily seen.

We thus conclude that the trends observed in the  $r_{in}$ - $\alpha$  plot are mostly resolution effects, in combination with intrinsic scatter in the inner slopes. The cusp problem is certainly genuine; it cannot plausibly be attributed to systematic errors in the data. LSB galaxies have shallow mass-density slopes implying that (i) the current CDM model, or more precisely the current generation of  $N$ -body models based on the CDM prescription, does not correctly describe structure at the scale of galaxies, or (ii) non-cosmological effects destroy the cusp. The second option reduces the elegance and predictive power of the CDM model.

## ACKNOWLEDGMENT

EdB thanks PPARC for Advanced Fellowship support.

## REFERENCES

- Adler D. S., Westpfahl D. J., 1996, *AJ*, 111, 735
- Athanassoula L., 2002, *ApJ*, 569, L83
- Begeman K. G., 1987, PhD thesis, University of Groningen
- Blais-Ouellette S., Amram P., Carignan C., 2001, *ApJ*, 121, 1952
- Bosma A., 1978, PhD thesis, University of Groningen
- Bosma A., Byun Y. I., Freeman K. C., Athanassoula E., 1992, *ApJL*, 400, L23
- Bullock J. S., Kolatt T. S., Sigad Y., Somerville R. S., Kravtsov A. V., Klypin A. A., Primack J. R., Dekel A., 2001, *MNRAS*, 321, 559
- Burkert A., 1995, *ApJ*, 447, L25
- de Blok W. J. G., Bosma A., 2002, *A&A*, 385, 816 (dBB02)
- de Blok W. J. G., McGaugh S. S., 1997, *MNRAS*, 290, 533
- de Blok W. J. G., van der Hulst J. M., Bothun G. D., 1995, *MNRAS*, 274, 235
- de Blok W. J. G., McGaugh S. S., van der Hulst J. M., 1996, *MNRAS*, 283, 18
- de Blok W. J. G., McGaugh S. S., Rubin V. C., 2001a, *AJ*, 122, 2396
- de Blok W. J. G., McGaugh S. S., Rubin V. C., Bosma, A., 2001b, *ApJ*, 552, L23 (dBBMR)
- de Vaucouleurs G., Freeman K. C., 1972, *Vistas in Astronomy*, 14, 163
- Deul E. R., van der Hulst J. M., 1987, *A&A Sup.*, 67, 509
- Dubinski J., Carlberg R. G., 1991, *ApJ*, 378, 495

- Firmani C., D'Onghia E., Avila-Reese V., Chincarini G., Hernández X., 2000, MNRAS, 315, L29
- Garrido O., Marcellin M., Amram P., Boulesteix J., 2002, A&A, 387, 821
- Jörsäter S., van Moorsel G. A., 1995, AJ, 110, 2037
- Kravtsov A. V., Klypin A. A., Bullock J. S., Primack J. R., 1998, ApJ, 502, 48
- Marchesini D., D'Onghia E., Chincarini G., Firmani C., Conconi P., Molinari E., Zacchei A., 2002, ApJ, 575, 801
- Matthews L. D., Wood K., 2001, ApJ, 548, 150
- McGaugh S. S., Rubin V. C., de Blok W. J. G., 2001, AJ, 122, 2381
- McGaugh S. S., Barker M. K., de Blok W. J. G., 2003, AJ, in press (astro-ph/0210641)
- Moore B., 1994, Nat, 370, 629
- Moore B., Governato F., Quinn T., Stadel J., Lake G., 1998, ApJL, 499, L5
- Moore B., Quinn T., Governato F., Stadel J., Lake G., 1999, MNRAS, 310, 1147
- Navarro J. F., Frenk C. S., White S. D. M., 1996, ApJ, 462, 563
- Navarro J. F., Frenk C. S., White S. D. M., 1997, ApJ, 490, 493
- Pisano D. J., Wilcots E. M., Elmegreen B. G., 1998, AJ, 115, 975
- Puche D., Carignan C., Bosma A., 1990, AJ, 100, 1468
- Salucci P., 2001, MNRAS, 320, L1
- Salucci P., Borriello A., 2001, MNRAS, 323, 285
- Swaters R. A., 1999, PhD thesis, University of Groningen
- Swaters R. A., Schoenmakers R. H. M., Sancisi R., van Albada T. S., 1999, MNRAS, 304, 330
- Swaters R. A., Madore B. F., van den Bosch F. C., Balcells M., 2003, ApJ, 583, 732
- van den Bosch F. C., Swaters R. A., 2001, MNRAS, 325, 1017
- Wechsler R. H., Bullock J. S., Primack J. R., Kravtsov A. V., Dekel A., 2002, ApJ, 568, 52
- Weldrake D. T. F., de Blok W. J. G., Walter F., 2003, MNRAS, 340, 12
- Zhao H. S., 1996, MNRAS, 278, 488

This paper has been typeset from a  $\text{\TeX}/\text{\LaTeX}$  file prepared by the author.